

MHD MATERIALS - SEED/SLAG INTERACTIONS AND EFFECTS

QUARTERLY PROGRESS REPORT

January 1 - March 31, 1981

Samuel J. Schneider  
Project Manager

Center for Materials Science  
U. S. Department of Commerce  
National Bureau of Standards  
Washington, D. C. 20234

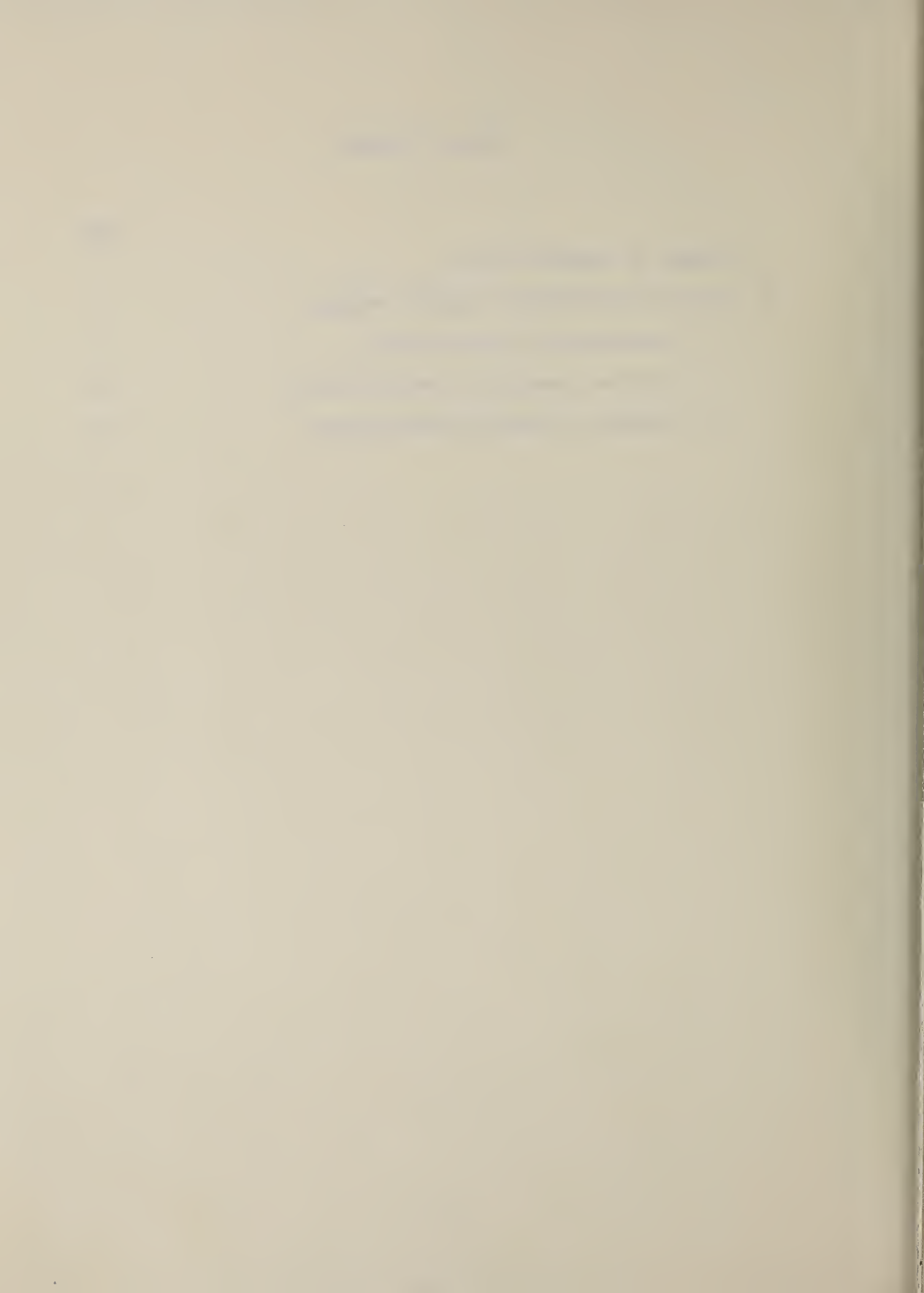
PREPARED FOR THE UNITED STATES  
DEPARTMENT OF ENERGY  
MHD OFFICE

"This report was prepared as an account of work sponsored by the United States Government. Neither the United States nor the United States Department of Energy, nor any of their employees, nor any of their contractors, subcontractors, or their employees, makes any warranty, express or implied, or assumes any legal liability or responsibility for the accuracy, completeness, or usefulness of any information, apparatus, product or process disclosed, or represents that its use would not infringe privately owned rights."



## TABLE OF CONTENTS

	<u>Page</u>
I. SUMMARY OF PROGRESS TO DATE . . . . .	1
II. DETAILED DESCRIPTION OF TECHNICAL PROGRESS . . . . .	2
1. Thermochemistry of Seed and Slag . . . . .	2
2. Electrical Conductivity and Polarization . . . . .	15
3. Corrosion of Downstream MHD Components . . . . .	25



## I. Summary of Progress to Date

### 1. Thermochemistry of Seed and Slag

An equation representing K-pressures covering the concentration ranges:  $K_2O$ , 3-14 wt%;  $CaO$ , 17-36 %; and  $Al_2O_3$ , 14-36 %: balance,  $SiO_2$  was fit to the data previously obtained from four component simplified "Western" channel slags. The equation uses three linear terms in concentration variables, a term in  $1/T$  and a constant. Increases in the  $K_2O$  and  $Al_2O_3$  concentrations of one percent predict increases in the K-pressure of 20 and -4 percent, respectively, while the effect due to  $CaO$  is negligible in this approximation. The standard deviation in the fit is 34 percent. Differences between the model and data are probably due to the assumption that bulk compositions represent the actual concentration in the slag solutions.

Experiments were continued in the system  $K_2O-CaO-Al_2O_3-SiO_2$ . Evidence suggests lack of significant solid solution within the compositional region investigated with the possible exception of  $KAlSi_2O_6$ .

### 2. Electrical Conductivity and Polarization

Data has been obtained to show a time-temperature relationship for obtaining a stable conductivity measurement in slag derived from coal from the Rosebud seam in Montana. Both AC and DC four probe conductivity measurements on this slag have been completed. A series of quenching experiments have also been completed but analysis of these experiments will be made later.

Four probe AC measurements were made on a sample of Na beta alumina, a known fast ion conductor, for comparison with the measurements made on the Rosebud slag also hypothesized to be at least a partially ionic conductor.

### 3. Corrosion of Downstream MHD Components

Specimens of A213-T22 steel tubes were exposed to  $K_2SO_4$  seeded fuel rich and oxygen rich hot gas streams. The wall temperatures of the specimens were maintained at 400 °C, 500 °C and 590 °C, respectively. SEM and EDX analysis were conducted on metallographically prepared sections of the specimens to determine the extent and the chemical nature of the reaction zone between the metal and the deposited salt coating. The distribution of the metal cations in the reaction zone is detailed and the extent of cation penetration into the deposited coating is described.

## II. Detailed Description of Technical Progress

### 1. Thermochemistry of Seed and Slag (E. R. Plante and L. P. Cook)

#### A. Vaporization Studies (E. R. Plante)

Progress: An objective of the current work is to obtain K-pressure data for selected compositions of the four component system,  $K_2O-CaO-Al_2O_3-SiO_2$ . These selected compositions correspond to the channel slag which would be produced by the interaction of seeded combustion gases with simplified "Western" coal ash. A second objective is to predict the K-pressure or  $K_2O$  activity in melts with compositions not too different from those studied by using the data base generated to develop an initially empirical model. Finally, it is planned to extend the model to other coal ash compositions, including additional components, such as  $Fe_2O_3$  and  $MgO$ . The basic use of such a model is to aid in determining the magnitude of seed loss to slag in MHD systems and to suggest the best method to minimize this effect.

Thus far, vapor pressure data have been determined for four different samples. Table 1 lists the initial mineral constituents and the starting and final composition in wt% of each of the four components. All vapor pressure measurements have been obtained using a Knudsen effusion, modulated beam mass spectrometric method.

During the current quarterly period, further studies and analysis of the KCAS-VP-4 measurements were made. As noted in the last report, the vapor pressures were approximately a factor of two higher than expected, and the decrease in volatility with composition was not as large as expected. We have now concluded that the initial analysis of the data was in error because of an incorrect weight loss during the first part of the experiment. In the final part of the experiment, the mass spectrometer constant was about a factor of two lower than in the earlier part and the use of a mass spectrometer constant weighted toward the latter value removes the apparent discrepancy.

Most effort during this period has been devoted to the development of an empirical model to predict K vapor pressures or activities of  $K_2O$  in molten slags. As a data base for this model, we have used the data obtained in the KCAS-VP-1, KCAS-VP-2 and KCAS-VP-3 experiments. Table 2 lists the results of treating the basic data in the simplest way, that is, separating the data into groups of limited composition and fitting the equation,

$$\log P_k = A/T + B \quad ,$$

by least squares. Table 2 is reproduced from a previous report. A few of the B terms have been altered slightly because of updated mass spectrometer constants in the final analysis. The basic data consists of 250 K-pressures at varying T, and compositions of  $K_2O$ ,  $CaO$ ,  $Al_2O_3$ , and  $SiO_2$ . An examination of the slopes in Table 2 shows that they are generally close to 17,000, except for those near the beginning of the

KCAS-VP-2 and the KCAS-VP-3 measurements. These lower slopes may be decreased by impurity evaporation (unreacted  $K_2CO_3$ ). Also, at the beginning of the KCAS-VP-1 experiment, the initial slopes are 20,000 and 19,000 until the  $K_2O$  bulk composition has been reduced to about nine wt%  $K_2O$ . These higher slopes may be due to increased  $K_2O$  concentration in the melt. Although all of the compositions have been calculated as though the sample is a homogeneous melt, this is probably not the case. Rather, it is more likely that a relatively homogeneous melt is in equilibrium with crystalline  $KAlSiO_4$ , which goes into solution as the temperature is increased with a resulting increase in both the  $K_2O$  and  $Al_2O_3$  concentrations.

In spite of the uncertainties in the composition variables, we have fit, by least squares, all of the data from the KCAS-VP-1, KCAS-VP-2, and KCAS-VP-3 measurements to an equation of the following form;

$$\log P \text{ (atm)} = A/T + B + C(\text{wt\% } K_2O) + D(\text{wt\% } CaO) + E(\text{wt\% } Al_2O_3) \quad .$$

The values of the coefficients and their standard deviations are listed in Table 3.

Table 3

Coefficients and Standard Deviations for Model Equation

Term	Value	Standard Deviation
A	-16794	176
B	5.228	0.173
C	7.887 E-2	0.309 E-2
D	1.741 E-3	3.318 E-3
E	-1.825 E-2	0.209 E-2

The coefficients in the equation show that each percent increase in the  $K_2O$  concentration increases the K-pressure by 20 percent, and each percent increase in the  $Al_2O_3$  concentration decreases the K-pressure by four percent. The effect of CaO on the K-pressure using this approximation is negligible. The standard deviation in the fit is 34 percent, while maximum deviations in individual points generally do not exceed 100 percent. Because most of the data used to fit this model equation are from data at lower concentration ranges (below about ten wt%  $K_2O$ ), it is to be expected that the model equation will predict too high a K-pressure for high "bulk concentrations" of  $K_2O$ , mainly because much of the  $K_2O$  at these compositions is tied up as  $KAlSiO_4$ . The formation of crystalline  $KAlSiO_4$  in the melt can be thought of as a buffering process, whereby the slag can increase its bulk  $K_2O$  content without as large an increase in K-pressure as would be observed if the  $K_2O$  were in solution.

Figures 1 and 2 are shown as an example of how well the model equation fits the data. Figure 1 shows the data from the KCAS-VP-1 measurements in the  $K_2O$  bulk composition range from 14.8-12.4 wt%  $K_2O$ .

The two reference lines show the K-pressures predicted by the model at 14.8 and 12.4 wt%  $K_2O$ , respectively. While it is clear that the data itself would give a steeper slope, the model representation is quite good. Figure 2 shows data for the KCAS-VP-2 data in the 11.4-10.7  $K_2O$  concentration range with the lines representing the upper and lower  $K_2O$  contents, respectively. Again the model representation is quite good. These examples are neither the best nor worst fit of the data.

Plans: Continue model development work, including application to other slag compositions. Supplement model data with further measurements as deemed necessary. Investigate effect of solution concentration data where available on the model.

Table 1

## Mineral Constituents and Composition of Vaporization Samples

Sample	Mineral Constituents (Wt%)	Initial/Final Composition Wt%			
		K <sub>2</sub> O	CaO	Al <sub>2</sub> O <sub>3</sub>	SiO <sub>2</sub>
KCAS-VP-1	KAlSiO <sub>4</sub> (49.8), Ca <sub>2</sub> SiO <sub>4</sub> (16.5)	14.8	27.5	22.2	35.5
	Ca <sub>2</sub> Al <sub>2</sub> SiO <sub>7</sub> (16.5), Ca <sub>3</sub> Si <sub>2</sub> O <sub>7</sub> (17.2)	1.6	31.8	25.7	40.9
KCAS-VP-2	KAlSiO <sub>4</sub> (28.6), KAlSi <sub>2</sub> O <sub>6</sub> (13.8)	11.5	17.6	33.7	37.2
	Ca <sub>2</sub> Al <sub>2</sub> SiO <sub>7</sub> (28.9), CaAl <sub>2</sub> Si <sub>2</sub> O <sub>8</sub> (28.7)	6.1	18.7	35.7	39.5
KCAS-CP-3	KAlSiO <sub>4</sub> (42.0), CaSiO <sub>3</sub> (58.0)	12.5	28.0	13.5	46.0
		1.8	31.4	15.2	51.6
KCAS-VP-4	KAlSiO <sub>4</sub> (66.9), Ca <sub>2</sub> SiO <sub>4</sub> (33.1)	19.9	21.6	21.6	37.0
		2.7	26.2	26.2	44.9

Table 2

## Slope, Intercept and Standard Deviations for K-Pressure Data

Expt Id	Wt% K <sub>2</sub> O	A	SD,A	B	SD,B
KCAS-VP-1					
3/13/80	14.8-12.4	-20047	391	8.062	.255
3/14/80	12.4- 9.3	-19071	524	7.196	.334
3/18/80	9.3- 7.2	-17429	452	5.976	.289
3/18/80	6.2- 4.8	-16372	210	4.986	.129
3/21/80	4.8- 4.0	-16896	279	5.207	.178
KCAS-VP-2					
5/14/80	11.4-10.7	-14632	434	4.200	.278
5/15/80	10.7- 8.6	-16366	180	5.097	.112
5/16/80	8.6- 6.5	-17571	257	5.656	.158
5/19/80	6.5- 6.2	-16606	526	4.992	.321
KCAS-VP-3					
8/13/80	12.5-10.8	-15052	775	4.983	.512
8/14/80	10.8-10.3	-17512	453	6.282	.298
8/14/80	10.3- 7.4	-15441	612	4.732	.374
8/15/80	7.4- 6.0	-16006	581	5.178	.362
8/15/80	6.0- 3.9	-15390	320	4.544	.197
8/18/80	3.9- 3.2	16948	801	5.417	.505

Figure 1. Potassium pressure vs.  $10^4/T$  for KCAS-VP-1 sample in the 14.8-12.4 wt%  $K_2O$  bulk composition range compared to lines from empirical model equation.

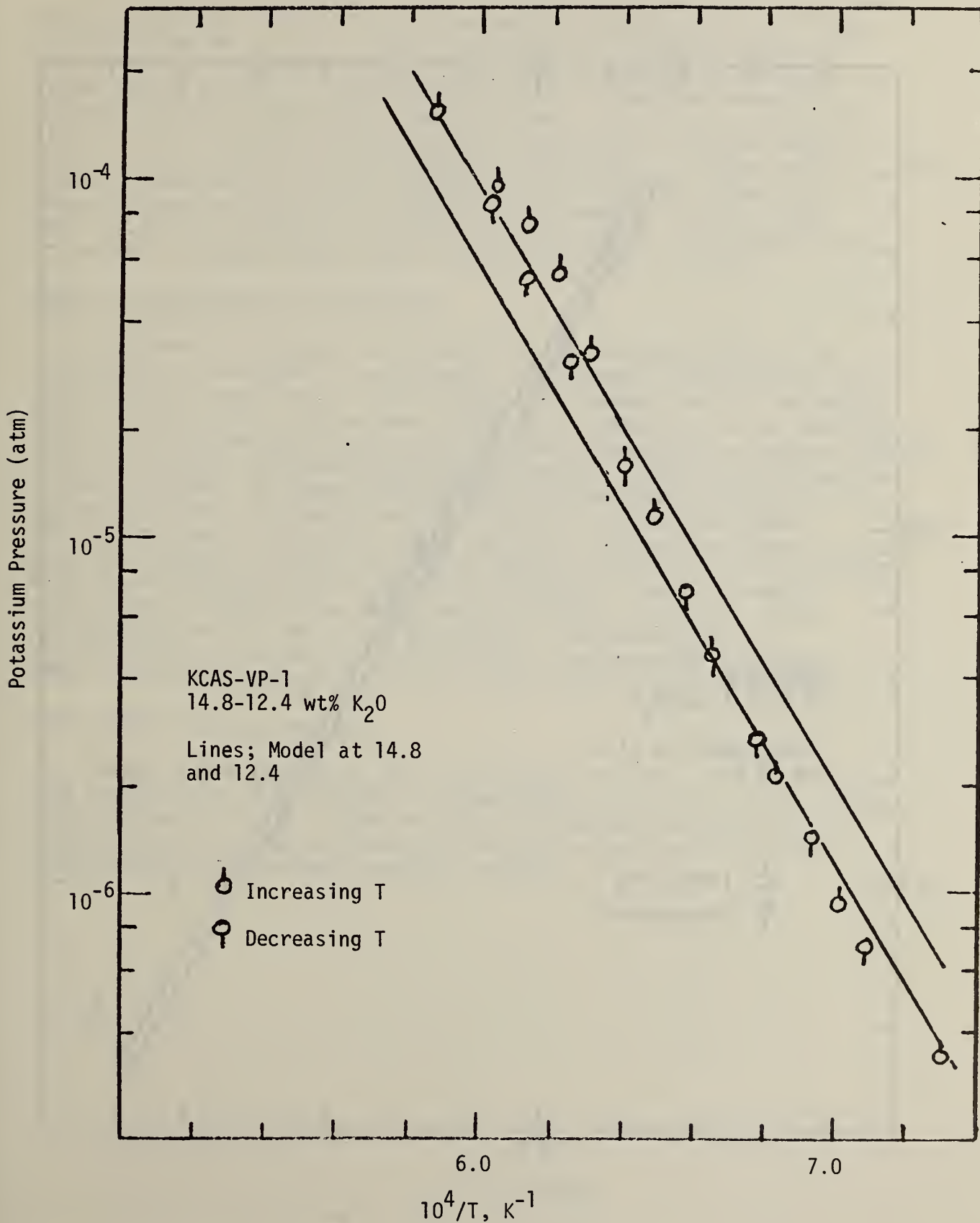
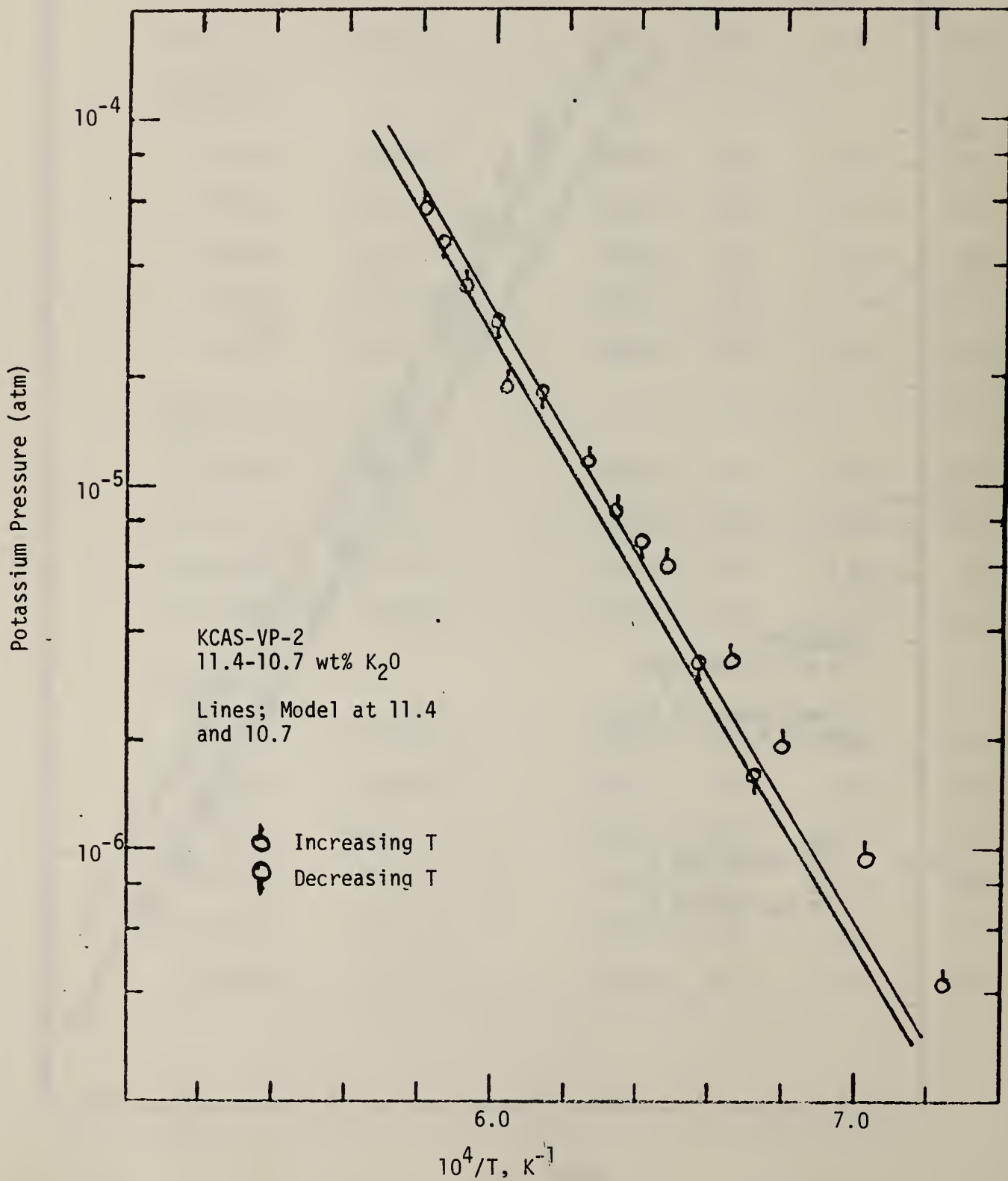


Figure 2. Potassium pressure vs.  $10^4/T$  for KCAS-VP-2 sample in the 11.4-10.7 wt%  $K_2O$  bulk composition range compared to lines from empirical model equation.<sup>2</sup>



## B. Phase Equilibria in the System $K_2O-CaO-Al_2O_3-SiO_2$ (L. P. Cook)

### Progress

In the previous quarterly report a series of three sets of experiments were outlined for verification of proposed subsolidus equilibria in the system  $K_2O-CaO-Al_2O_3-SiO_2$ . Briefly these are: 1) 1000 hr subsolidus equilibrations in which mixtures of the four crystalline phases corresponding to each of 13 proposed equilibrium volumes are heated for extended periods with periodic regrinding and x-ray analysis; 2) solid state tie line reactions using unstable combinations of phases which in principle should react to produce the stable pair; 3) glass crystallization experiments in which completely melted samples of the four phase volumes are quenched to produce glass, powdered, sealed in Pt capsules and crystallized at subsolidus temperatures. For convenience a diagram of proposed subsolidus relations is shown in Figure 1.

### 1000 Hour Subsolidus Equilibrations

Specimens of extended equilibrations have been examined by x-ray diffraction to determine if any changes in parameters have occurred which might indicate significant solid solution. In general lattice parameter shifts corresponding to more than  $.05^\circ 2\theta$  ( $CuK\alpha$  radiation) can be detected easily. During the last quarter  $KAlSi_3O_8$  was successfully synthesized hydrothermally, making additional experiments possible. Results are summarized in Table 1 below. In general there appears to be little evidence for the existence of solid solutions from results of these experiments, and the four phase assemblages shown in figure 1 appear to be substantiated with the possible exception of  $KAlSi_2O_6/KAlSi_3O_8/3Al_2O_3 \cdot 2SiO_2/CaAl_2Si_2O_8$ . Mullite and  $KAlSi_2O_6$  in this assemblage apparently react to produce  $\alpha-Al_2O_3$  and an unidentified phase whose principle x-ray lines do not correspond to any of the silica polymorphs. The possibility of a hydrated phase cannot be ruled out, as this experiment was performed under a confining pressure of 7500 psi with  $\sim 5$  wt %  $H_2O$  in the capsule.

### Solid State Tie Line Reactions

Table 2 below summarizes data accumulated to date on two-phase tie line verification at 1200-1300 °C. Essentially all the tie lines involving  $KAlSiO_4$  shown in figure 1 have now been verified with the exception of  $KAlSiO_4/CaAl_2Si_2O_8$ , which appears to be complicated by solid solution relationships (see previous quarterly report).

Now that  $\text{KAlSi}_3\text{O}_8$  is available as a starting material, additional reactions will be tested in the near future to verify  $\text{KAlSi}_2\text{O}_6/\text{CaAl}_2\text{Si}_2\text{O}_8$  and  $\text{KAlSi}_2\text{O}_6/\text{CaSiO}_3$ . Verification of  $\text{KAlSi}_3\text{O}_8/\text{CaAl}_2\text{Si}_2\text{O}_8$  and  $\text{KAlSi}_3\text{O}_8/\text{CaSiO}_3$  will be done hydrothermally.

### Glass Crystallization Experiments

Glasses from 8 of the 13 four phase volumes in figure 1 have been crystallized, as shown in Table 3 below. It was necessary to crystallize assemblages with  $\text{KAlSi}_3\text{O}_8$  hydrothermally ( $\sim 5$  wt % water added; 7500 psi confining pressure) due to the low temperatures required to maintain subsolidus conditions. Glasses from the remaining five volumes have not been successfully prepared due to their high melting nature and high viscosity, despite heating to temperatures approaching 1900 °C. Results of experiments in Table 3 are consistent with four-phase volumes indicated in figure 1. The occurrence of cristobalite instead of quartz is not surprising; however its lattice parameters do not indicate substantial solid solution. Lattice parameters of potassium aluminosilicates from certain of the glass crystallization experiments are slightly larger than pure end members. The exact significance of this is at present uncertain.

### Plans

Complete experiments on subsolidus  $\text{K}_2\text{O}-\text{CaO}-\text{Al}_2\text{O}_3-\text{SiO}_2$ . Measure compositions of invariant melts from four phase volumes. Begin experiments with iron-containing compositions.

Table 1. Summary of Extended Four-Phase Equilibrations.

Four Phase Volume	Cumulative Treatment (Temp °C) (Time, hr)		New Phases?	Evidence for Solid Solution?
$\text{KAlSiO}_4/\text{Al}_2\text{O}_3/CaAl_{12}O_{19}/CaAl_2Si_2O_8$	1200	1000	No	No
$\text{KAlSiO}_4/CaAl_{12}O_{19}/Ca_2Al_2SiO_7/CaAl_2Si_2O_8$	1200	1000	No	No
$\text{KAlSiO}_4/KAlSi_2O_6/Ca_2Al_2SiO_7/CaAl_2Si_2O_8$	1200	1000	No	No
$\text{KAlSiO}_4/KAlSi_2O_6/Ca_2Al_2SiO_7/CaSiO_3$	1200	1000	No	No
$\text{KAlSiO}_4/KAlSi_2O_6/Al_2O_3/CaAl_2Si_2O_8$	1200	1000	No	No
$\text{KAlSi}_2O_6/Al_2O_3/3Al_2O_3 \cdot 2SiO_2/CaAl_2Si_2O_8$	1200	1000	No	No
$\text{KAlSi}_2O_6/Ca_2Al_2SiO_7/CaAl_2Si_2O_8/CaSiO_3$	1200	1000	No	No
$\text{KAlSi}_2O_6/KAlSi_3O_8/CaAl_2Si_2O_8/CaSiO_3$	700 ( $P_{H_2O} = 7500$ psi)	316	mon. $CaSiO_3$	No
$\text{KAlSi}_2O_6/KAlSi_3O_8/3Al_2O_3 \cdot 2SiO_2/CaAl_2Si_2O_8$	700 ( $P_{H_2O} = 7500$ psi)	316	$Al_2O_3 +$ unident. phase (mullite and possibly $KAlSi_2O_6$ disappeared)	No
$\text{KAlSi}_3O_8/3Al_2O_3 \cdot 2SiO_2/CaAl_2Si_2O_8/SiO_2$	700 ( $P_{H_2O} = 7500$ psi)	316	No	No
$\text{KAlSi}_3O_8/CaAl_2Si_2O_8/CaSiO_3/SiO_2$	700 ( $P_{H_2O} = 7500$ psi)	316	No	No
$\text{KAlSiO}_4/Ca_3Si_2O_7/Ca_2Al_2SiO_7/CaSiO_3$	1200	1000	No	No
$\text{KAlSiO}_4/Ca_3Si_2O_7/Ca_2SiO_4/Ca_2Al_2SiO_7$	1200	1000	No	No

Table 2. Summary of Tie Line Reactions.

Tie Line	Alternative Starting Materials	Tie Line Verified?
$\text{KAlSiO}_4/\text{Ca}_2\text{Al}_2\text{SiO}_7$	$\text{Ca}_2\text{SiO}_4/\text{KAlSi}_2\text{O}_6/\text{CaAl}_{12}\text{O}_{19}$	Yes
$\text{KAlSiO}_4/\text{Ca}_2\text{SiO}_4$	$\text{CaO}/\text{KAlSi}_2\text{O}_6$	Yes
$\text{KAlSiO}_4/\text{Ca}_3\text{Si}_2\text{O}_7$	$\text{Ca}_2\text{SiO}_4/\text{KAlSi}_2\text{O}_6$	Yes
$\text{KAlSiO}_4/\text{CaSiO}_3$	$\text{Ca}_3\text{Si}_2\text{O}_7/\text{KAlSi}_2\text{O}_6$	Yes
$\text{KAlSiO}_4/\text{CaAl}_{12}\text{O}_{19}$	$\text{Ca}_2\text{Al}_2\text{SiO}_7/3\text{Al}_2\text{O}_3 \cdot 2\text{SiO}_2/\text{KAlO}_2$	Yes
$\text{KAlSi}_2\text{O}_6/\text{Ca}_2\text{Al}_2\text{SiO}_7$	$\text{KAlSiO}_4/\text{CaAl}_2\text{Si}_2\text{O}_8/\text{CaSiO}_3$	Yes

Table 3. Summary of Glass Crystallization Experiments.

Four Phase Volume	Heat Treatment (Temp °C) (Time, hr)		Phases Detected	Evidence for Solid Solution?
$\text{KAlSiO}_4/\text{CaAl}_{12}\text{O}_{19}/\text{Ca}_2\text{Al}_2\text{SiO}_7/\text{CaAl}_2\text{Si}_2\text{O}_8$	1200	100	Same	No
$\text{KAlSiO}_4/\text{KAlSi}_2\text{O}_6/\text{Ca}_2\text{Al}_2\text{SiO}_7/\text{CaAl}_2\text{Si}_2\text{O}_8$	1200	100	Same	No
$\text{KAlSiO}_4/\text{KAlSi}_2\text{O}_6/\text{Ca}_2\text{Al}_2\text{SiO}_7/\text{CaSiO}_3$	1200	100	Same	No
$\text{KAlSi}_2\text{O}_6/\text{Ca}_2\text{Al}_2\text{SiO}_7/\text{CaAl}_2\text{Si}_2\text{O}_8/\text{CaSiO}_3$	1200	100	Same	Slight increase in unit cell of $\text{KAlSi}_2\text{O}_6$
$\text{KAlSi}_2\text{O}_6/\text{KAlSi}_3\text{O}_8/\text{CaAl}_2\text{Si}_2\text{O}_8/\text{CaSiO}_3$	700 ( $P_{\text{H}_2\text{O}} = 7500$ psi)	316	$\text{KAlSi}_2\text{O}_6/\text{KAlSi}_3\text{O}_8/\text{CaAl}_2\text{Si}_2\text{O}_8/\text{monoclinic CaSiO}_3$	No
$\text{KAlSi}_3\text{O}_8/\text{CaAl}_2\text{Si}_2\text{O}_8/\text{CaSiO}_3/\text{SiO}_2$	700 ( $P_{\text{H}_2\text{O}} = 7500$ psi)	316	Cristobalite/ $\text{CaAl}_2\text{Si}_2\text{O}_8/\text{KAlSi}_3\text{O}_8/\text{monoclinic CaSiO}_3$	No
$\text{KAlSiO}_4/\text{Ca}_3\text{Si}_2\text{O}_7/\text{Ca}_2\text{Al}_2\text{SiO}_7/\text{CaSiO}_3$	1200	100	Same	Slight increase in unit cell of $\text{KAlSiO}_4$
$\text{KAlSiO}_4/\text{Ca}_2\text{SiO}_4/\text{Ca}_3\text{Si}_2\text{O}_7/\text{Ca}_2\text{Al}_2\text{SiO}_7$	1200	100	Same	Slight increase in unit cell of $\text{KAlSiO}_4$

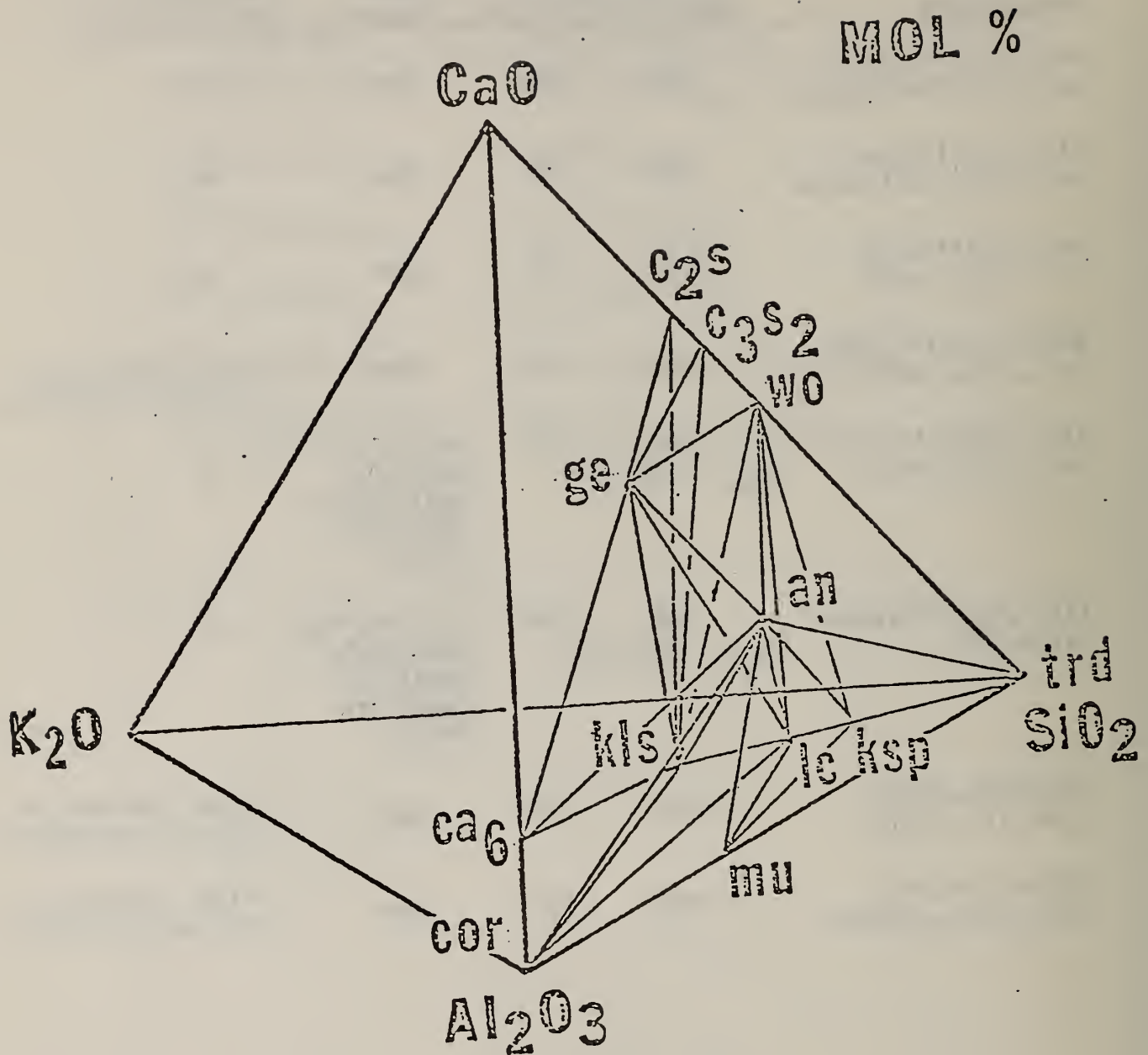
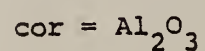
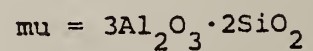
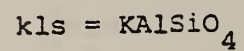
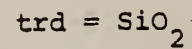
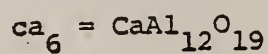
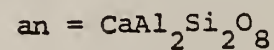
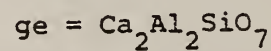
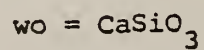
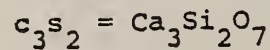
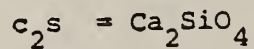


Figure 1.



## Electrical Conductivity and Polarization (W. R. Hosler)

### Progress

#### Introduction

In the last quarterly report (October-December 1980), AC and DC four probe measurements on coal slag derived from the Rosebud seam in Montana were described. This slag contains a minimal amount of iron (approximately 4 w/o) compared to a typical Eastern slag (approximately 12-16%).

During this quarter, work has continued on the investigation of the conductivity mechanisms in the slag with low iron content. Emphasis has been placed on the near equilibrium state required for a stable conductivity at a given temperature and the relationship of the specific impedance of resistance measured between the probe sets. This relationship when observed over a frequency of range 40 kHz down to zero Hz (DC) can possibly give information about the conducting process in the slag. The physical properties of the near equilibrium state were established by quenching stabilized samples with subsequent analysis by SEM and XRD techniques.

In the last quarterly report, measurements on a sample of  $ZrO_2$  which is an oxygen ion conductor were described. These measurements were unsatisfactory in showing the polarization effects of ionic conductivity because the platinum electrodes as well as the near-electrode sample area were oxygen ion-exchanging with the oxygen in the ambient atmosphere. A set of measurements (AC & DC four probe) has been completed on Na-beta alumina received from Dr. John A. Bast of the General Electric Co. in Schenectady, NY. Beta alumina properly prepared is a nearly completely ionic conductor. The conducting ion, Na, K, Ag, etc. moves through the material with higher than usual ionic mobility and research at a number of laboratories indicates that the material shows promise as a solid electrolyte for battery or other applications. For our measurements, the purpose was again to establish the viability of using a combination of four probe AC & DC measurements to establish a true bulk resistivity as well as to show that these measurements can give some information as to the conductivity mechanisms of the material.

#### Slag Conductivity

An elemental analysis of the slag from Rosebud seam coal is given in the last quarterly report. Pollina and Larsen<sup>1,2</sup> have done extensive measurements on slag from this coal but using a somewhat different experimental technique. The slag for this experiment has been altered by adding 20%  $K_2SO_4$  to the melt in order to give a potassium content more representative of slag residing in a functioning MHD generator. Potassium rejection, however, occurs when the sulfate is added so that a considerable amount less of potassium ends up in the final material. In this case analysis for potassium in the doped material was 5.8 w/o before the electrical measurements were carried out and 5.0% after the measurements were completed so that loss of potassium during the course of the measurements was not appreciable. The potassium rejection upon initial doping is much less in an Eastern slag such as that obtained from the Bow, NH steam generating plant where the calcium content is low.

During the course of the electrical measurements, much more careful attention was paid to attaining a stable conductivity at a given temperature than had been done previously. Figure 1 shows time required at a given temperature necessary for the conductivity to change by less than 1%/hour. These changes were continuously monitored by the data acquisition system. Methods for acquiring the data were described in previous quarterly reports.

Figure 2 shows the conductivity of this Western slag with 5 w/o potassium as a function of inverse temperature. Both AC (40 Hz) and DC data are shown and the measurements were done in an air atmosphere. At each temperature point, stabilization times were allowed to correspond to those shown in figure 1. At temperatures above 1200 °C the AC and DC data are nearly the same but at lower temperatures the frequency dependence of the conductivity becomes larger. Extrapolation to zero or low frequency brings the AC and DC conductivities into near agreement. Specific impedances were calculated for all probe sets. Definition of these probe sets was given in Quarterly Report July - September 1980, but a brief description will be given again as an aid in reading this report. The slag is held in an alumina crucible through which 4 probes are inserted into the slag sample. The top probe labeled 1, and the bottom probe labeled 4, are electrodes through which current is introduced into the sample. Probes 2 and 3, second and third from the top, carry no current and are potential sensors along the sample length. Polarization effects when present should be observed at current carrying probes only, especially when non ion exchanging electrodes are used with an ionically conducting species. SEM micrographs together with EDX analysis show no iron or potassium incorporated in the bulk platinum of any one of the four probes. Specific impedances were calculated between all probe sets. Specific impedance is the measured impedance (resistance) between a probe set multiplied by the area and divided by the distance between the set. Thus  $Z_{12} = Z \cdot A / d_{12}$ ,  $Z_{23} = Z \cdot A / d_{23}$  and  $Z_{34} = Z \cdot A / d_{34}$ . The area A remains the same throughout the sample length. The distances between probe sets is  $d_{12}$ ,  $d_{23}$  and  $d_{34}$ . Z is the measured impedance between each set.  $Z_{23}$  is then the sample resistivity as measured at a particular frequency. If  $Z_{12}$  does not vary with frequency over a frequency range then capacitive reactance effects do not play a significant role in determining the total impedance and the impedance is non-reactive. Figure 3 is a plot of  $Z_{23}$  vs. frequency for several temperatures. At high temperature (above 1200 °C) there is no frequency dependence at least below 10 kHz so AC (40 Hz) and DC data agree quite well as shown in figure 2. The frequency dependence of  $Z_{12}$  and  $Z_{34}$  is very small also for temperatures above 1200 °C but the magnitudes are always larger than  $Z_{23}$  at a given temperature.

Figure 4 is a plot of the  $F_{34}(V)$  values for this slag function of temperature. The origin and significance of this value is given in Quarterly Report July - September 1980. This value remains relatively constant for the 40 Hz measurement over the temperature range plotted. Since the variation in  $V_{23}$  and  $V_{34}$  with frequency is small, the variation of  $F_{34}(V)$  is also small with frequency. The DC value of  $F_{34}(V)$  also shown on the same figure, increased significantly above 1300 °C which indicates that ionic conductivity is playing a significant roll in the total conductivity and that polarization effects are significant. This effect does not appear to be as pronounced as that in the Bow, NH slag described in previous quarterly reports.

This slag conductivity sample was sectioned into four pieces, each containing a probe. These sections were examined using a scanning electron microscope with EDX spectroscopy. X-ray diffraction analysis was done on pieces from several sections. The spectrum was identical for each section which indicates that there were no gross differences in composition along the sample length. The pattern was very strong in anorthite ( $\text{CaAl}_2\text{Si}_2\text{O}_8$ ) or potash feldspar ( $\text{KAlSi}_3\text{O}_8$ ) and leucite ( $\text{KAlSi}_2\text{O}_4$ ) with a small amount of hercynite ( $\text{FeAl}_2\text{O}_4$ ). A very small amount of another unknown phase was also indicated. EDX analysis showed areas that appeared to have a crystalline nature. Lighter areas always had Fe, Al and Mg combinations which suggest an magnesia-iron alumina spinel but none was detected in the XRD spectrum. In these areas generally Ti and Ca were present. Other areas showed Al, Si, K and Ca combinations. Micrographs of the sample along with EDX spectra will be given in a later report.

### Quenching Experiments

One of the purposes of the electrical measurements and analysis is to try to correlate the electrical conductivity with a component in the sample at a particular temperature. One way to do this would be to quench each sample very rapidly to low temperature just after the electrical measurement at an elevated temperature and then make a possible correlation between conductivity and component materials and physical state. This would be a very time consuming process requiring attachment of the platinum electrodes through the alumina crucible walls thus constructing a new cell for each temperature point. As shown in figure 1, a certain time is required at every temperature for the conductivity to become stabilized. A furnace was so arranged that samples of slag in alumina crucibles identical to conductivity samples but without the probes could be dropped into a water bath. The furnace was programmed to hold a set temperature for the time shown in figure 1 after which a sample was quenched; the programmed temperature dropped to another set temperature for a specified time, another sample quenched and so on. A series of quenched samples were prepared in this manner. These samples are in the process of being prepared for SEM and XRD examination and will be reported later.

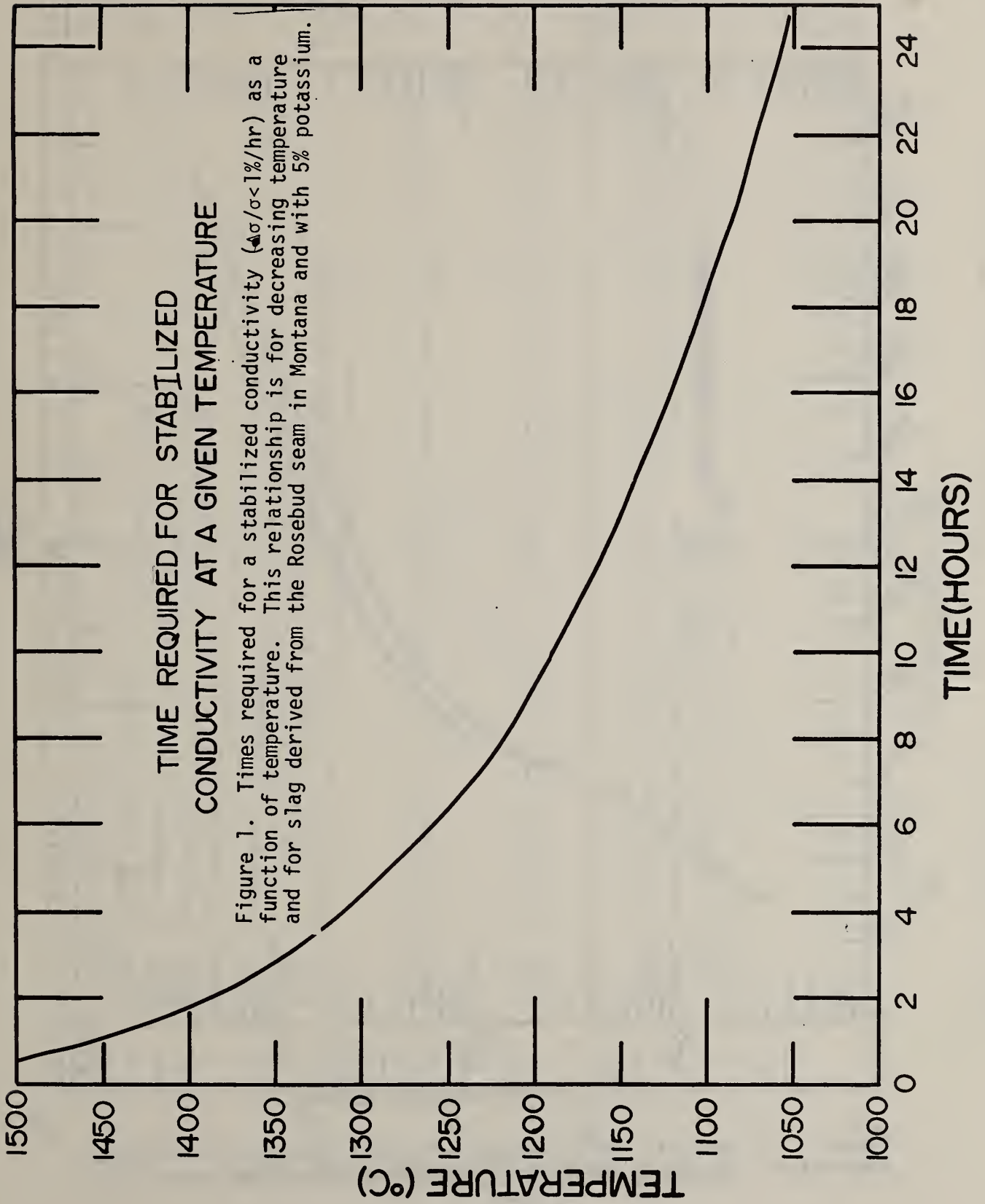
### Conductivity Measurements on Na-beta Alumina

The beta alumina sample was prepared by cutting the bulk material which was in the form of a tube 27 mm in diameter and 23 mm long into samples 23 mm long, 3 to 4 mm wide and 1.5 mm thick (tube wall thickness). XRD spectra in the tube material showed it to be all beta alumina. Leads were attached in the usual manner, i.e., by drilling holes for the four probes along the length of the sample and attaching the platinum lead out wires with spongy platinum peened into the holes around the lead. Figure 5 shows a plot of the specific admittance ( $1/Z_{23}$ ) times temperature at 40 Hz vs. reciprocal of absolute temperature.  $Z_{23}$  is the resistance between the center two probes (conductivity probes) multiplied by the cross sectional area (A) and divided by the distance between the probes  $d_{23}$ . This should represent the true bulk conductivity of the material if the impedance is independent of frequency in this range. The data shown in figure 5 agree very well with that given by Wittingham and Huggins<sup>3</sup> where the sodium ion

transport in beta alumina was measured using reversible solid electrodes. Their measurements were made, however, on single crystals and in a direction perpendicular to the c axis. The material used in this experiment was high density ceramic. Figure 6 is a plot of  $Z_{23}$  as a function of frequency for several temperatures. It can be readily seen that the specific impedance remains constant over the frequency range from 40 Hz to 40 kHz for this probe set. On the other hand the specific impedances measured between probe sets 1 and 2 and between 3 and 4, i.e.,  $Z_{12}$  and  $Z_{34}$ , did not remain constant with frequency but increased by nearly an order of magnitude with decreasing frequency from 40 kHz to 40 Hz. This indicates that a capacitive reactance  $x_C = \frac{1}{\omega C}$  was a contributing factor to the total impedance between these probe sets. This behavior is in contrast to the impedances  $Z_{12}$  and  $Z_{34}$  as measured in the slag sample discussed previously where these values did not vary significantly with frequency but the magnitudes were higher. As might be expected then, from the increase in impedance as the frequency is lowered even to 40 Hz, a DC measurement between these probe sets is not possible. The current carrying probes act like the plates of a condenser where charge builds up until breakdown occurs. The final result is that this material cannot be used to demonstrate the comparison of F(V) values discussed previously because DC values cannot be measured due to the fast ion conductivity. On the other hand it does demonstrate that even in a fast ion conductor such as beta alumina, a four probe AC measurement with non-ion exchanging electrodes gives accurate electrical conductivity values.

### References

1. R. Pollina and R. Larsen, 17th Symposium on Eng. Aspects of MHD, C.6.1., Stanford University, Stanford, CA (March 27-29, 1978).
2. R. Pollina, W. Anderson, R. Larsen, 7th Intl. Conf. on MHD Electrical Power Generation, D-8, Vol. 1, p. 226-232, MIT, Cambridge, MA (June 16-20, 1980).
3. M. S. Wittingham and R. A. Huggins, J. of Chem. Phys. 54, No. 1, 414 (1971).



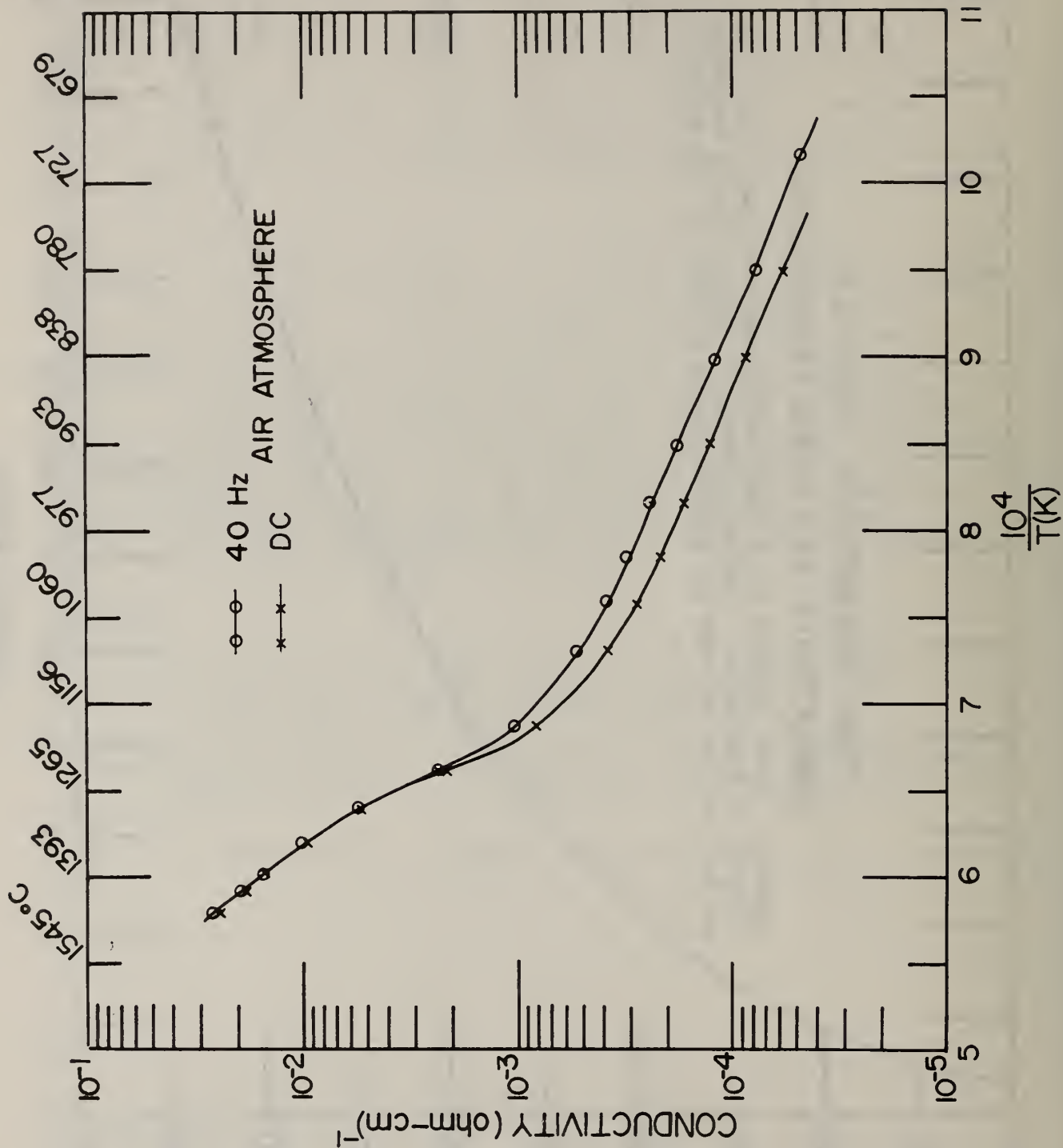


Figure 2. Electrical conductivity in air as a function of reciprocal temperature. 40 Hz AC and DC data are shown. Slag from Rosebud coal.

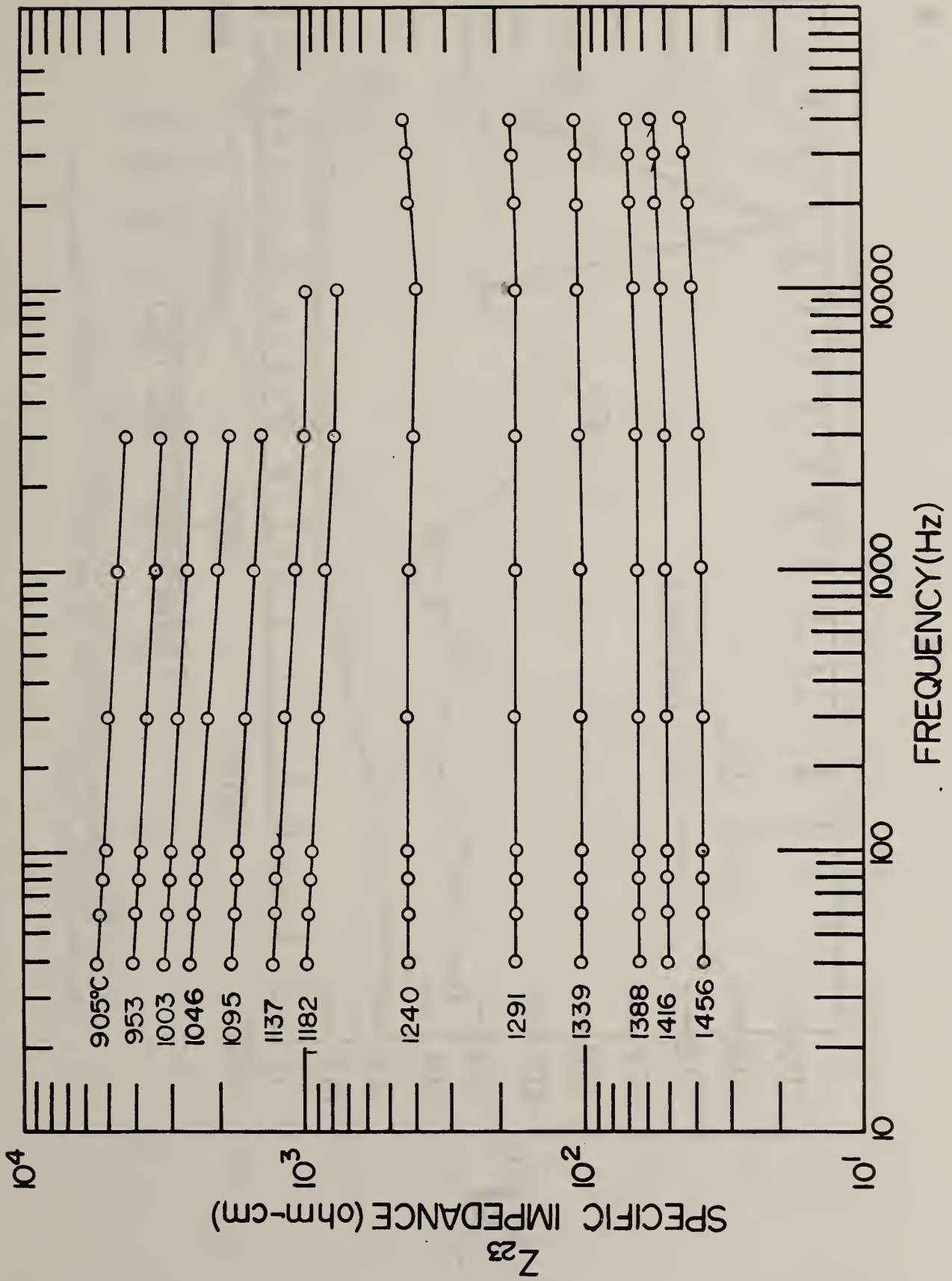


Figure 3. Specific impedance ( $Z_{23}$ ) vs. frequency for several temperatures. Slag from Rosebud coal.

22  $F_{34}$  (V)

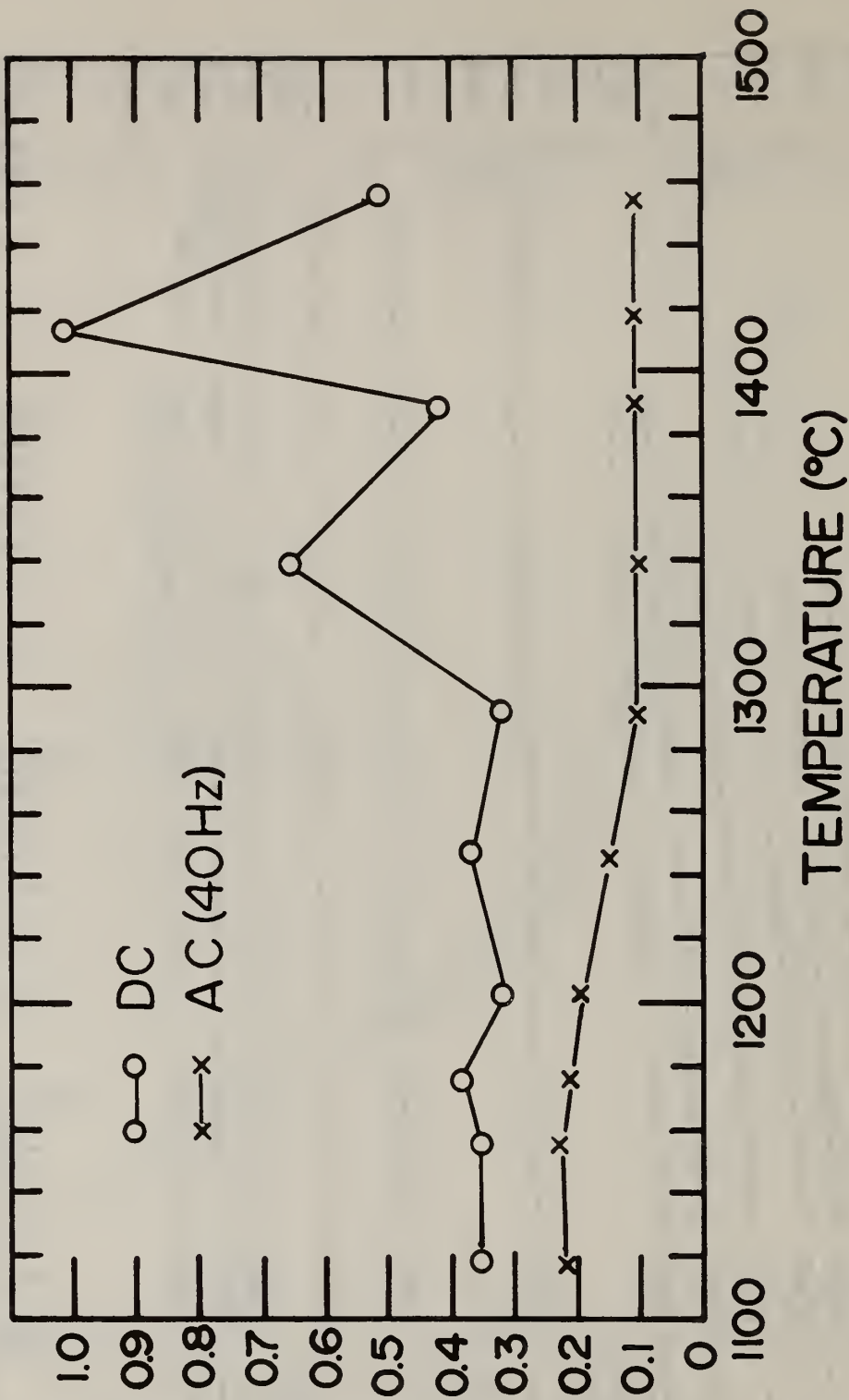


Figure 4.  $F_{34}$  (V) values (40 Hz AC and DC) as a function of temperature. Slag from Rosebud coal.

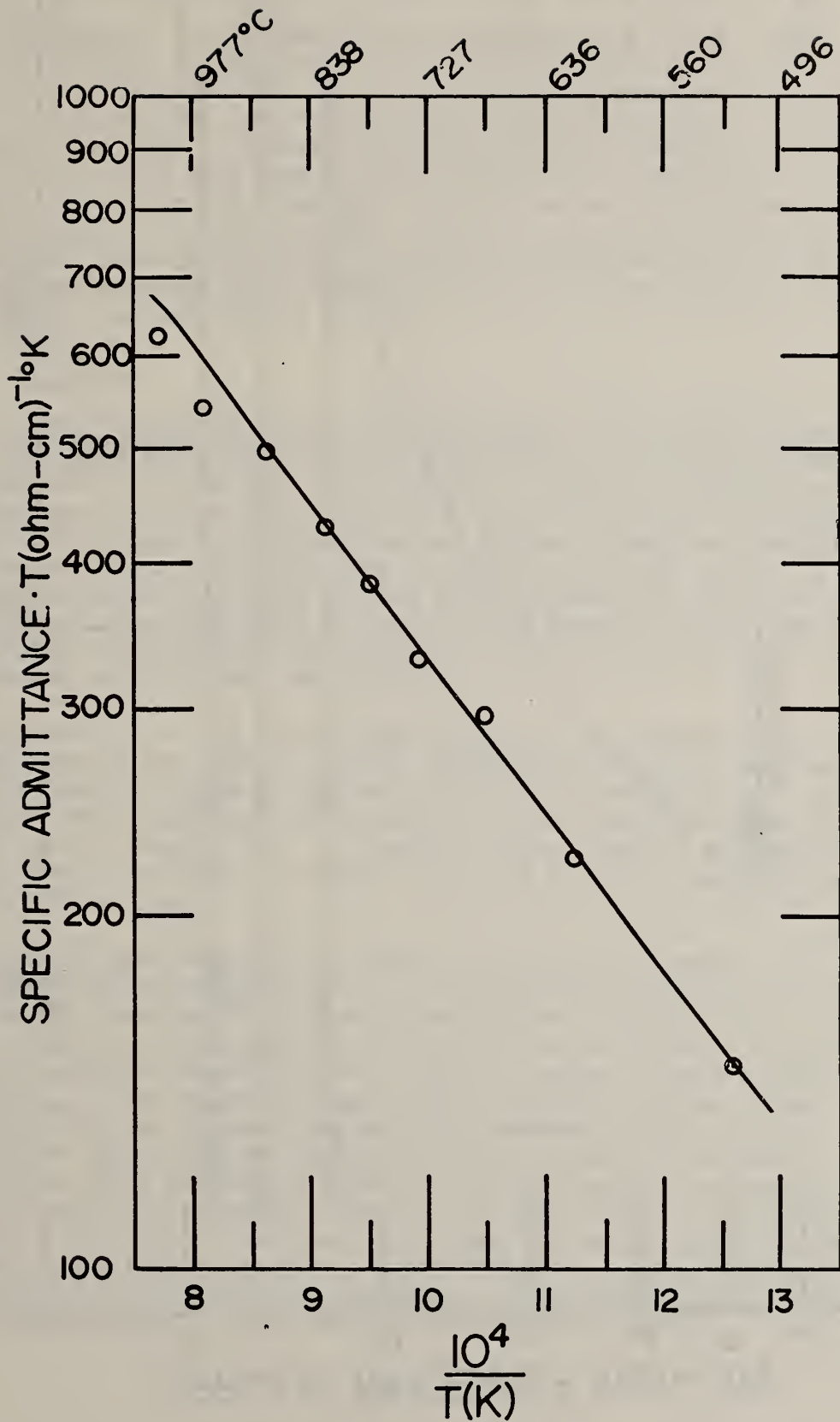


Figure 5. Specific admittance (conductivity) · T vs. reciprocal temperature for Na-beta alumina. These measurements were done in air.

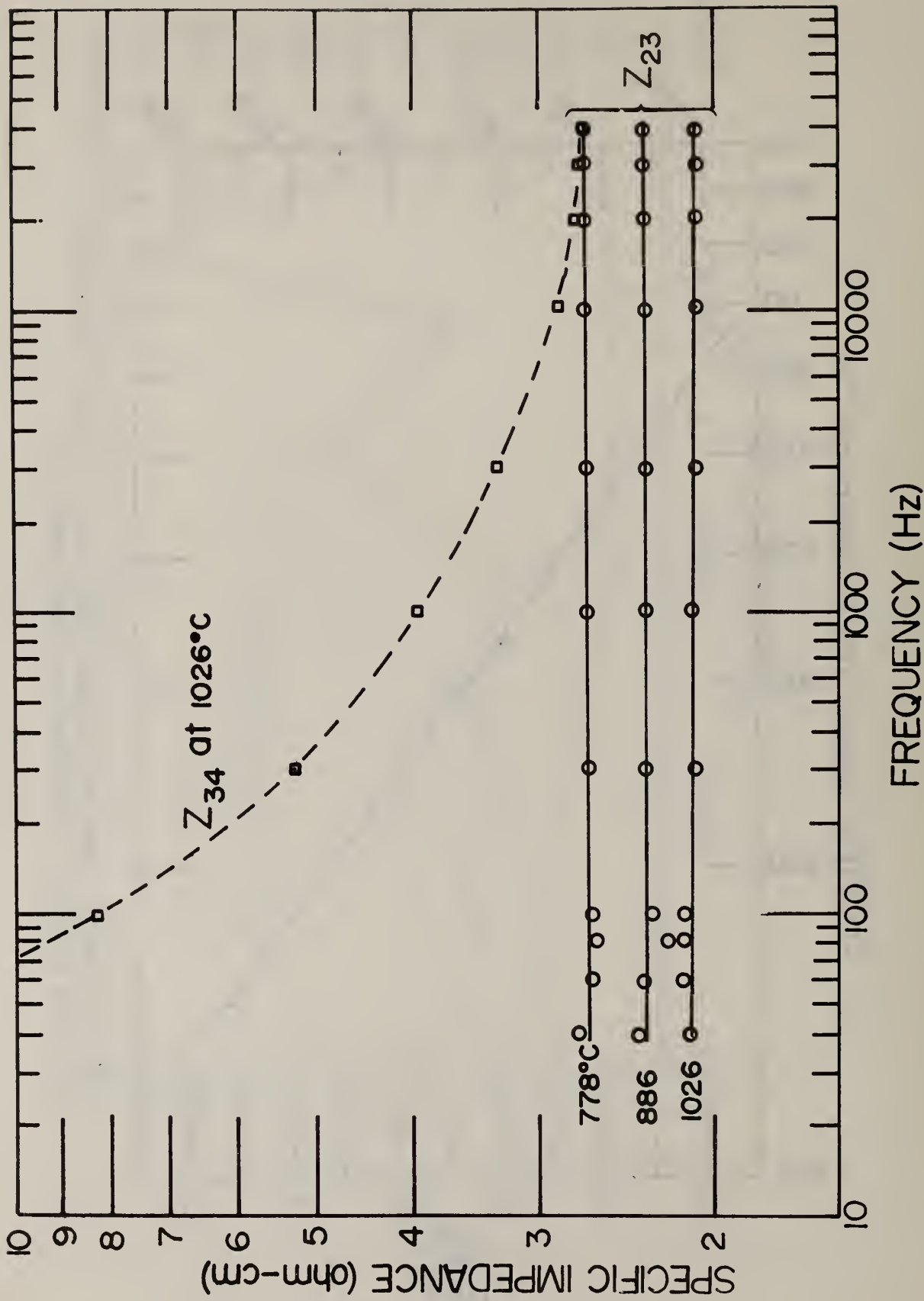


Figure 6. Specific impedance  $Z_{23}$  and  $Z_{34}$  of Na-beta alumina as a function of frequency for several temperatures.

### 3. Corrosion of Downstream MHD Components (J. Smit, 561 and C. D. Olson, 565)

Introduction: The examination and evaluation of various metals subjected to a corrosive hot gas stream is being undertaken to determine the suitability of the materials to function in heat exchangers in the bottoming unit of a combined magnetohydrodynamic (MHD)-steam power electrical generating system. Selected metal specimens are being exposed to fuel rich and oxygen rich, metal salt seeded hot gas streams which reproduce some of the expected characteristics of the harsh environment existing downstream in the heat exchanger region of the steam bottoming plant. The resistance to corrosion and erosion of the materials in the described environments gives an indication, to a first approximation, as to their potential suitability for service.

#### 1. Progress

A. Characterization of ASTM A213-T22 Steel: Samples of boiler pressure tubing, ASTM A213-T22 containing 1.95% chromium, 0.44% molybdenum, 0.44% manganese, 0.12% carbon, 0.015% sulphur, 0.35% silicon with the balance iron, were analyzed with respect to surface condition and homogeneity. The specimens were characterized: a) in the as received condition, b) after cleaning, and c) after exposure to a seeded hot gas stream. A scanning electron microscope (SEM) with an energy dispersive x-ray analyzer (EDX) was used to conduct the analysis on sections taken from the specimens and prepared for examination, with slight variation, using standard metallographic techniques.

The material, in the as received condition, was covered with a smooth, semi-gloss black coating. Closer examination, Fig. 1, revealed surface striations with some voids paralleling the longitudinal axis of the tube. Higher magnification, Fig. 2, shows a rather rough but seemingly homogeneous top layer, however, Fig. 3, shows particles embedded in the surface. EDX analysis of the area in general indicated no gross abnormalities in the bulk composition.

All of the specimens in the series covered by this report were cleaned to constant weight prior to test in an ultrasonic bath at 50 °C in a 10% by weight ammonium citrate solution adjusted to neutral pH. The surface of the cleaned specimen, Fig. 4, showed the same type of striation as seen on the uncleaned surface as well as areas of varying contrast, Fig. 5. Closer examination of these discolored regions, Figs. 6 and 7, showed also the presence of particles embedded in the surface. The chemical composition of these particles varied from the bulk and a slight chemical shift was also observed in the bulk material surrounding the particles, Figs. 8 and 9. Other areas were observed, Figs. 10, 12 and 15 where particles are embedded in the bulk and whose composition varies from that of the bulk, Figs. 11, 13, 14, 16 and 17. These areas of inhomogeneity have been found throughout the sample. The possibility exists that corrosion may be enhanced in these regions, manifested as pitting or crack propagation.

It is not known if these particles were embedded in the melt or embedded during fabrication. However, knowledge of their existence aids in understanding the presence of unexpected metal cations such as Cu, Zn and Al in the EDX examination of specimens exposed to the hot gas streams. Their presence also complicates attempts to understand the behavior of the system.

B. Examination of the ASTM A213-T22 Steel: The boiler pressure tubing, (about 12.4 mm in diameter, wall thickness about 1.5 mm) was cut into 0.30 m lengths for test purposes. Six specimens in all were used to complete this series. Each tube was thoroughly cleaned as described. At the midpoint of the tube a Pt/Pt10%Rh thermocouple was welded in place to monitor tube wall temperature. The thermocouple output signal is also used in a feed back loop to control the tube wall temperature by adjusting the cooling air flow rate.

The tubular specimens were subjected to either an oxygen rich or propane rich hot gas stream seeded with  $K_2SO_4$  (see Table 1). All specimens were exposed, exclusive of apparatus warm up and cool down, for a period of approximately four hours with seeding of 250 g of salt occurring in the first 25 minutes. Six specimens were exposed under these general conditions, two at 590 °C, two at 500 °C, and two at 400 °C. The gas stream temperature, in all cases, was held at approximately 1300 °C as indicated by a Pt/Pt10%Rh thermocouple placed in the vicinity of the test specimen in the hot gas stream. The test specimens, following the exposure runs, were analyzed using an SEM/EDX system.

Table 1.

Specimen	Material	Corrosive Salt	Tube Wall T °C	Gas Stream State
Cr 1.	ASTM A213, T-22	$K_2SO_4$	590	O <sub>2</sub> rich
Cr 4.	ASTM A213, T-22	$K_2SO_4$	500	O <sub>2</sub> rich
Cr 3.	ASTM A213, T-22	$K_2SO_4$	400	O <sub>2</sub> rich
Cr 2.	ASTM A213, T-22	$K_2SO_4$	590	Propane rich
Cr 5.	ASTM A213, T-22	$K_2SO_4$	500	Propane rich
Cr 6.	ASTM A213, T-22	$K_2SO_4$	400	Propane rich

C. SEM/EDX Analysis of the Metal-Salt Deposit Region: Test specimens were removed from the test apparatus upon cool down to approximately 40 °C and encapsulated immediately in epoxy to prevent any possibility of contamination and to reduce the possibility of hydration occurring in the salt coatings. Metallographic specimens were selected from the

tubular specimen, 10 mm from the midpoint. These specimens were cut, ground, and polished using nonaqueous media and stored in evacuated desiccators prior to SEM/EDX analysis.

Test specimens Cr-1 and Cr-2 were exposed at 590 °C, Cr-4 and Cr-5 at 500 °C, and Cr-3 and Cr-6 at 400 °C. All samples exhibited similar salt deposit characteristics in that the coating was generally a compact deposit of  $K_2SO_4$ . A few areas were found where dissociation of the coating deposit occurred leaving high potassium or high sulfur concentrations.

Figures 18-20 (Cr-1, Cr-4, Cr-3) oxygen rich show the coating formed in the hot gas environment seeded with  $K_2SO_4$ . These samples retain a very thick salt deposit ranging from 2.3 mm to 3.2 mm in thickness on the leading edge of the tube surface facing the gas stream. The fume deposit, underside of the tube is approximately 0.2 mm in thickness (Table 2). This type of deposit is typical of that produced by  $K_2SO_4$  seeding in  $O_2$  rich environment and has been seen on previous test specimens.

Table 2. Coating Deposition on Tubular Specimens.

Specimen	Top (mm)	Bottom (mm)
Cr-1	2.3	0.18
Cr-4	3.2	0.2
Cr-3	3.2	0.2
Cr-2	0.65	0.32
Cr-5	0.82	0.33
Cr-6	0.47	0.31

Figures 21-23 (Cr-2, Cr-5, Cr-6) show the result of  $K_2SO_4$  seeding in a fuel rich hot gas stream. The leading edge is much thinner ranging from 0.5 mm to 0.8 mm. These samples also exhibit a thicker fume deposit region than the oxygen rich environment, approximately 0.3 mm.

An evaluation of specimens Cr-1 (Fig. 18) and Cr-2 (Fig. 19) can be made simultaneously. Both samples were seeded using  $K_2SO_4$  with wall temperatures maintained at 590 °C, however Cr-1 was in an oxygen rich fuel environment and Cr-2 was in a fuel rich environment. The variations in the salt deposit can readily be observed with the oxygen gas stream specimen (Cr-1) exhibiting a top deposit of 2.3 mm and a fume deposit 0.2 mm. The fuel rich gas stream sample (Cr-2) shows a top deposit of 0.65 mm and a fume region of 0.3 mm.

The bulk of both coatings is predominately K + S, however, some areas are depleted with one or the other species.

The corrosion process exhibited in both samples seems to follow the same general corrosion mechanism. In sample Cr-1 (oxygen rich) at the leading edge, salt-steel interface (Figs. 24-31) we find the bulk steel followed by a metal reaction band region where high chromium is found at the metal reaction band-bulk steel interface. Associated with this region is lower iron (compared to the bulk) and traces of potassium and sulfur. Chromium is found to be depleted towards the top of the metal corrosion band and not found to penetrate into the salt corrosion band area. Iron is found to be the major cation in the metal corrosion band and also is found to penetrate into the salt corrosion band region above it. Potassium and sulfur increase in concentration from the metal corrosion band/steel interface region towards the salt coating. Figures 32-36 shows an area where the corrosion bands can be seem to overlap. Depletion of the iron is observed through the use of x-ray mapping. Figures 37-41 support the previous data, indicating: a) bulk steel, b) high chromium, iron, low potassium and sulfur, c) iron, low chromium, potassium and sulfur, d) iron, potassium, sulfur, e) potassium, sulfur, iron, f) potassium and sulfur.

In Cr-1 (Fig. 42), the metal corrosion or reaction can be observed at the drip zone salt/steel interface region. The darker band region, as analyzed by EDX, Figs. 43-47, indicate that the corrosion mechanism in the drip zone region follows that of the upper part of the tube. We find concentrations of the cations as follows: a) bulk steel (iron, chromium), b) high chromium, iron, low sulfur and potassium, c) low chromium, iron, sulfur, potassium, d) iron, sulfur, potassium, e) sulfur, potassium, iron, f) potassium and sulfur. SEM/EDX analysis seems to indicate a preferential leaching of the metal cations from the bulk material in a somewhat orderly fashion.

The iron cations appear to be the more reactive species in the steel. The iron is preferentially leached by the corrosive salt from the bulk while chromium appears to form a concentrated layer in the corrosion zone of the metal. Whether this layer retards corrosion growth or accelerates it is not clear, however, from previous work chromium has been found not to be as mobile as iron.

Figure 48 shows a portion of the fume deposit region where the corrosive process appears to be evident. Figure 49 shows the iron x-ray map of the area indicating lower iron on the tube edge (iron migration into salt) and Figure 50 shows potassium penetration into the steel. EDX (Figs. 51, 52) supplements (Figs. 49,50) analysis of cation migration in this area.

In sample Cr-2, fuel rich, at the leading edge of the ASTM A213 T-22 steel (Figs. 53-60) we again find the bulk steel followed by a reaction zone area. As in the oxygen rich sample (Cr-1), there appears using EDX analysis to be distinctive corrosion banding. The corrosive process in the fuel rich environment seems to follow the same general order as found in the oxygen rich environment. The ordering is such that: a) bulk steel (iron, chromium), b) high chromium, iron, low sulfur and potassium, c) low chromium, iron, potassium, sulfur, d) iron, potassium, sulfur, e) potassium, sulfur, iron, f) potassium and sulfur.

It should be noted that in Fig. 53, Cr-2 there appears to be mechanical separation in the corrosion zone (i.e., cracking). This apparent lifting from the bulk represents a scaling of the tube surface.

The drip zone region, Fig. 61, exhibits a reaction band area similar to the leading edge, including what appears to be scale formation breaking off of the bulk composition. Figure 62 shows the area under higher magnification while Figs. 63-71 indicate the same cation pattern in the reaction zone as found at the leading edge.

The fume region (Fig. 72) exhibits a reaction area including cracking or scaling of the upper tube surface. Photomicrographs of x-ray mapping show cation concentrations of iron (Fig. 74), potassium (Fig. 73), sulfur (Fig. 75), and chromium (Fig. 76). Again iron is found to drop off in concentration near the edge of the metal reaction band (top of tube surface) where it reacts and penetrates the salt deposit. Figure 77 is a higher magnification of this region, EDX analysis (Figs. 78-86) indicate that the fume region corrosion is similar to that of the leading edge and drip zone.

At lower temperatures of 500 °C and 400 °C corrosion is still observed in the ASTM A213, T-22 steel. In Cr-4 (Fig. 19) 500 °C, oxygen rich hot gas stream, corrosion as well as scaling is observed (Fig. 87). Analysis (Figs. 88-90) of this corrosion region follow previous observations found in sample Cr-1. In Cr-5 (500 °C, fuel rich hot gas stream) corrosion again follows previous observation (Figs. 91-97). In Cr-3 (400 °C, oxygen rich hot gas stream) and Cr-6 (400 °C, fuel rich hot gas stream) analysis has shown similar cation positioning and layering, though to a lesser degree.

## 2. Conclusion

The variances between fuel rich and oxygen rich hot gas environments in the presence of  $K_2SO_4$  are minimal. Corrosion and scaling of ASTM A213, T22 steel seem to occur readily in both instances. Both systems seem to exhibit a discernable corrosion area, however, the fuel rich system seems to advance corrosion. Comparative measurements of reaction band areas (Table 3) seem to indicate that more degradation of the steel tube is taking place under a reducing environment, i.e., fuel rich, at the higher temperatures. Reaction zones seem to be comparable at the lower, i.e. 500 °C and 400 °C, temperatures.

Table 3.

Sample	Reaction Zone		Thickness in $\mu\text{m}$ Fume Deposit
	Top	Drip Zone	
Cr-2 590 °C	45	19	24
Cr-5 500 °C	--	5	4
Cr-6 490 °C	4*	4	5
Oxygen Rich Series			
Cr-1 590 °C	14	19	28
Cr-4 500 °C	14	40	10
Cr-3 400 °C	7	3	5

\*  $4\mu\text{m}$  reaction depth during test translates to approximately 9 mm/year

Both systems indicate the same general corrosion banding and cation movement from the bulk steel to the corrosive salt deposit. If the corrosion is translated to longer periods of time this steel will not stand up to the demand as a heat exchange material in the environments anticipated in the MHD-steam bottoming generator.

Plans: 1. Continue SEM/EDX analysis of arc-plasma sprayed coatings initiated previously to include additional cycling tests in both air and forming gas. 2. Conduct exposure tests on arc plasma sprayed mild steel tubing.

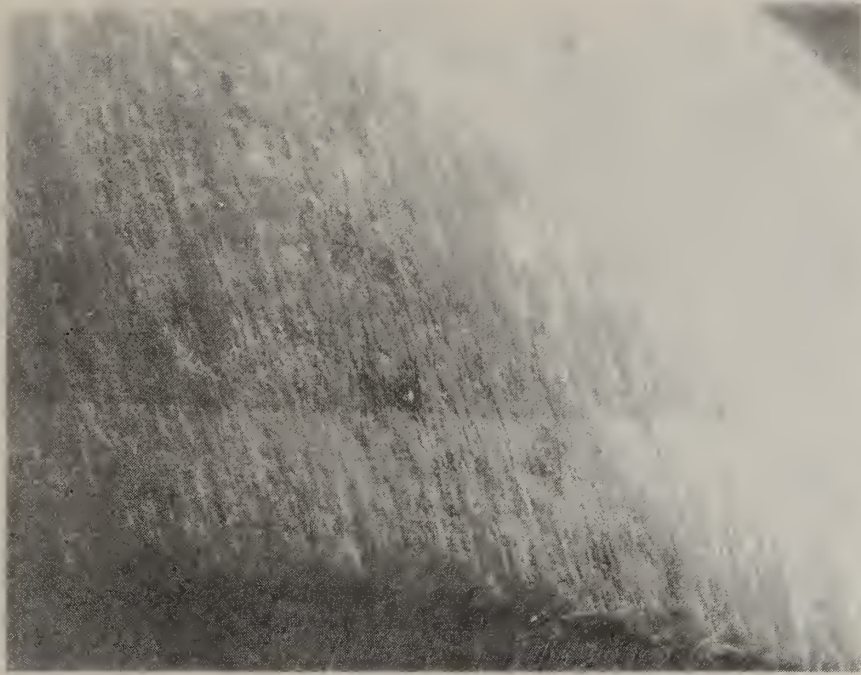


Fig. 1 SEM photomicrograph, 24x showing surface of ASTM 213-T22 steel as received.



Fig. 2 SEM photomicrograph, 125x showing same region as in Fig. 1.  
Note Striations



Fig. 3 SEM photomicrograph 2430x showing particles imbedded in the surface.



Fig. 4 SEM photomicrograph, 20x, showing surface of ASTM 213-22T steel after cleaning.

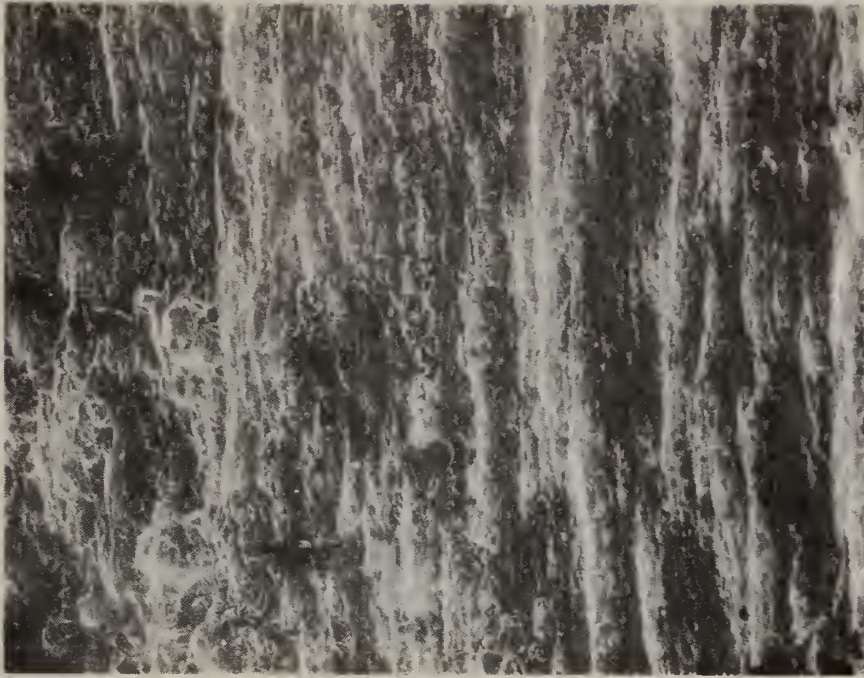


Fig. 5 SEM photo micrograph, 100x, showing same region as in Fig. 4. Note Striations.



Fig. 6 SEM photomicrograph, 25x, showing surface of ASTM 213-22T steel after cleaning. Note imbedded particle.



Fig. 7 SEM photomicrograph, 115x, of mid region of Fig. 6. Note imbedded particle. Lettered regions correspond to labeled EDX spectra Figs. 8 and 9.

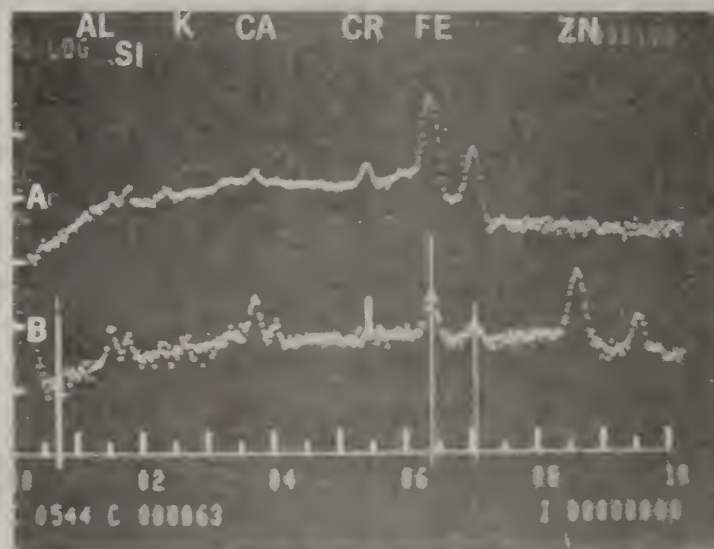


Fig. 8 EDX spectra of regions A and B of Fig. 7 showing species present in the embedded particle and species present adjacent to it. Species positions and designations of all spectra in this section of this report are as indicated above.

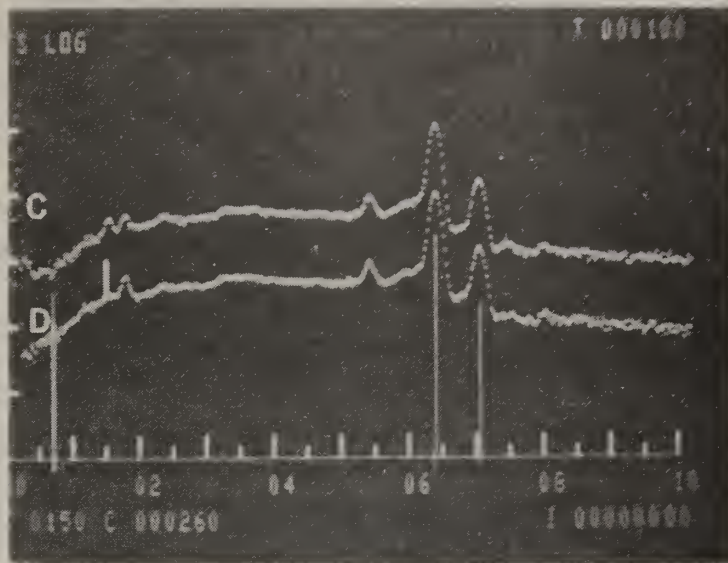


Fig. 9 EDX spectra of regions C and D of Fig. 7 showing species in bulk and in region adjacent to the embedded particle.



Fig. 10 SEM photomicrograph, 1140x showing presence of another embedded particle. This one of high Si content. Lettered regions correspond to labeled EDX spectra of Fig. 11.

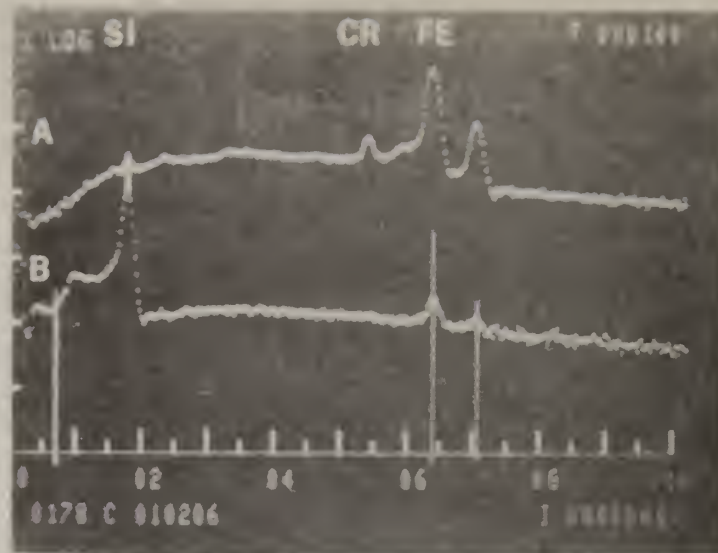


Fig. 11 EDX spectra of regions A and B of Fig. 10 showing species present in the bulk and the presence of Si in the embedded particle.



Fig. 12 SEM photomicrograph 1170x showing presence of still another embedded particle. Lettered regions correspond to labeled EDX spectra of Figs. 13 and 4.

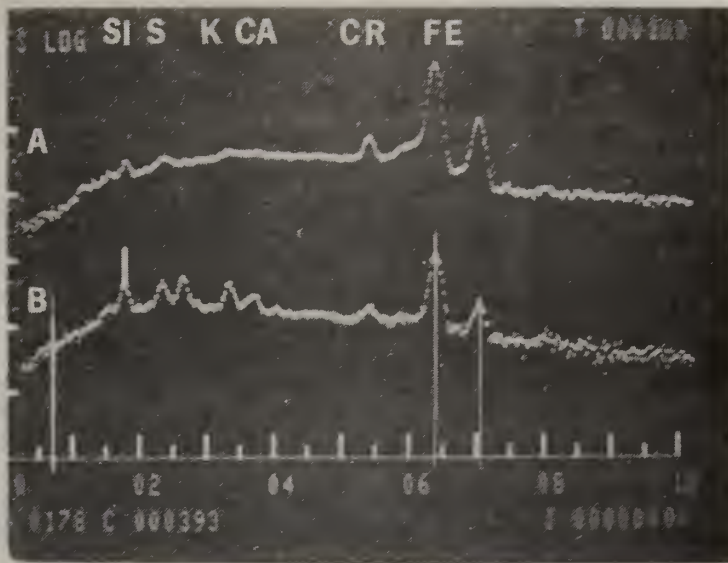


Fig. 13 EDX spectra of regions A and B of Fig. 12 showing the composition of the particle compared to the bulk.

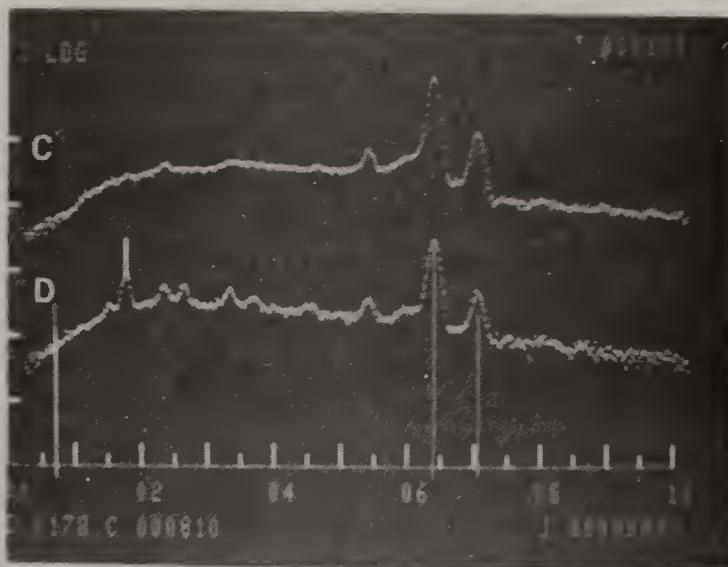


Fig. 14 EDX spectra of regions C and D of Fig. 12 showing the composition of the particle compared to the bulk.



Fig. 15 SEM micrograph 1150x of an embedded particle in the bulk. Lettered regions correspond to the labeled EDX spectra of Figs. 16 and 17.

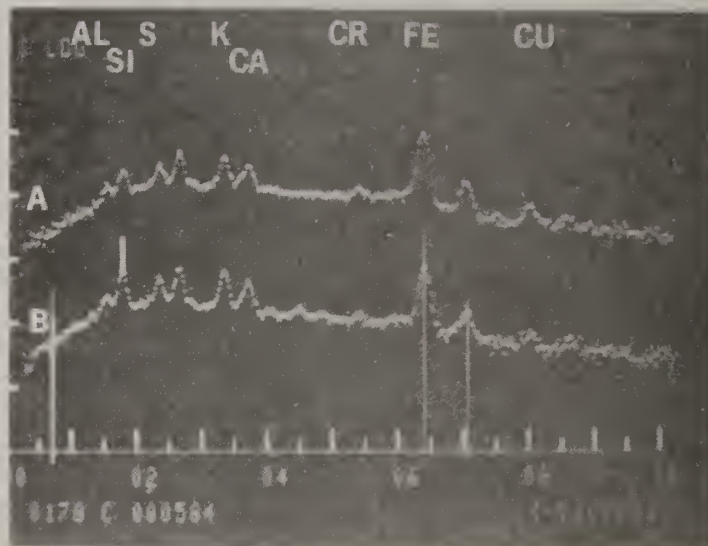


Fig. 16 EDX spectra of regions A and B of Fig. 15 showing presence of several species with a near absence of chromium. Species positions and designations of all spectra in this section of this report are as indicated above.

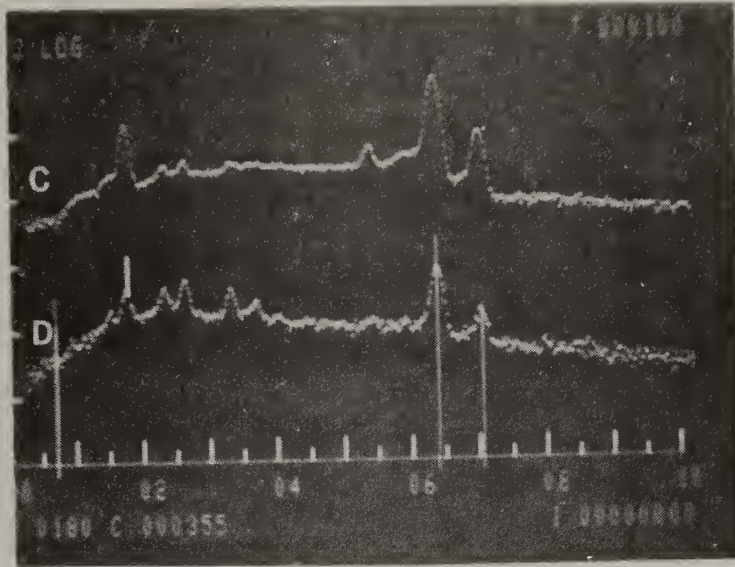


Fig. 17 EDX spectra of regions C and D of Fig. 15 showing high Si peak.

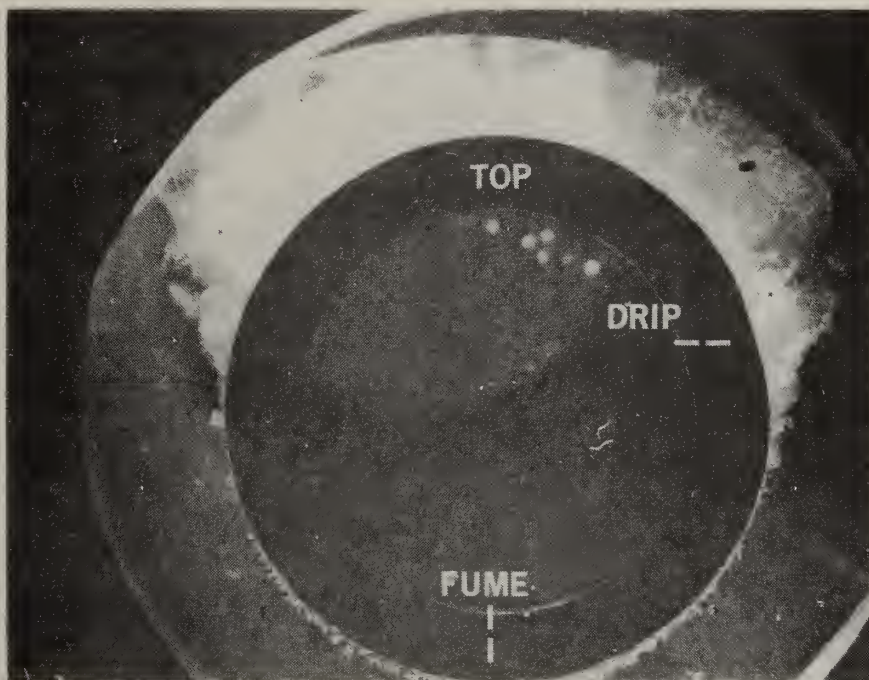


Fig. 18 Optical micrograph of a section of ASTM 213-22T steel tubing after exposure to an oxygen rich hot gas stream seeded with  $K_2SO_4$ . Tube temperature  $590^\circ C$ . Note deposit on upper surface of tube. Top position faces gas stream.

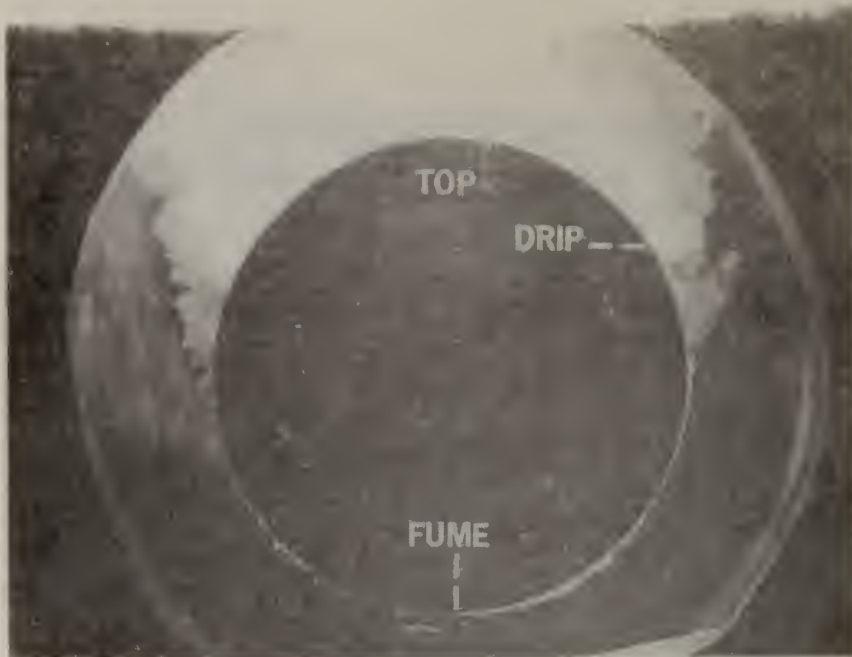


Fig. 19 Optical micrograph of a section of ASTM 213-22T steel tubing after exposure to an oxygen rich hot gas stream seeded with  $K_2SO_4$ . Tube temperature  $500^\circ C$ .



Fig. 20 Optical micrograph of a section of ASTM 213-22T steel tubing after exposure to an oxygen rich hot gas stream seeded with  $K_2SO_4$ . Tube wall temperature  $400^\circ C$ .

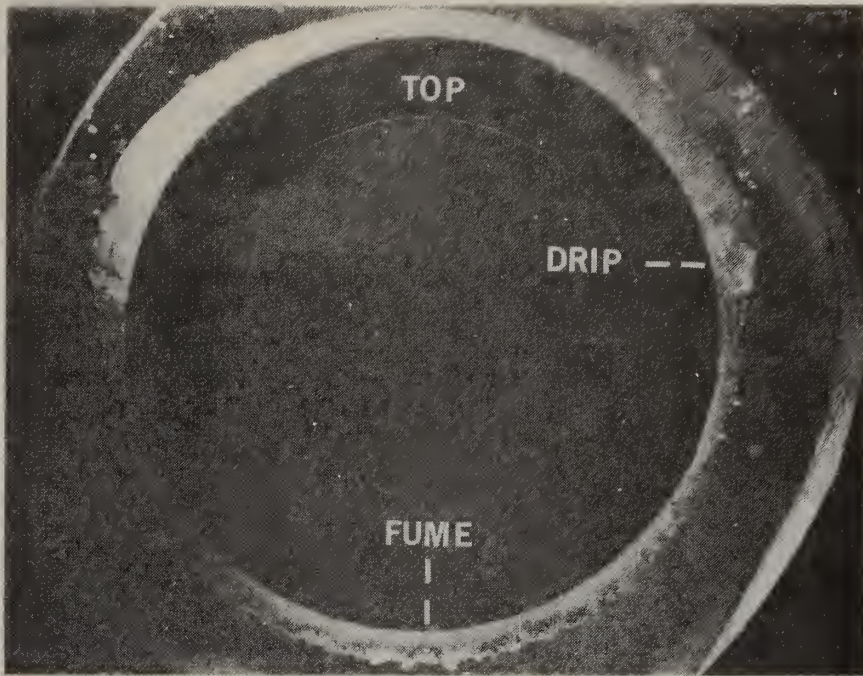


Fig. 21 Optical micrograph of a section of ASTM 213-22T steel tubing after exposure to a fuel rich hot gas stream seeded with  $K_2SO_4$ . Tube wall temperature  $590^\circ C$ . Note relatively thin deposit on upper surface of tube.

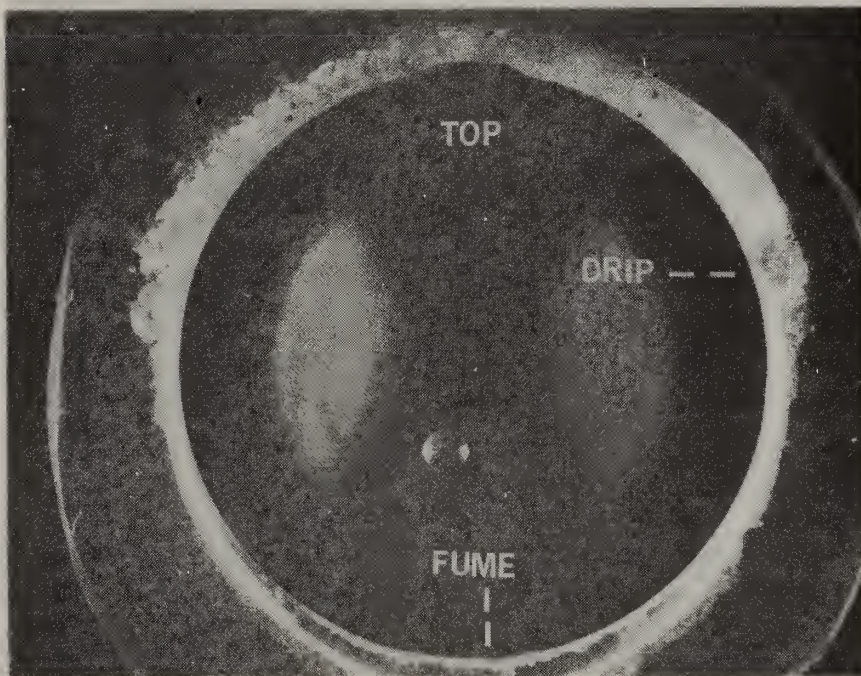


Fig. 22 Optical micrograph of a section of ASTM 213-22T steel tubing after exposure to a fuel rich hot gas stream seeded with  $K_2SO_4$ . Tube wall temperature  $500^\circ C$

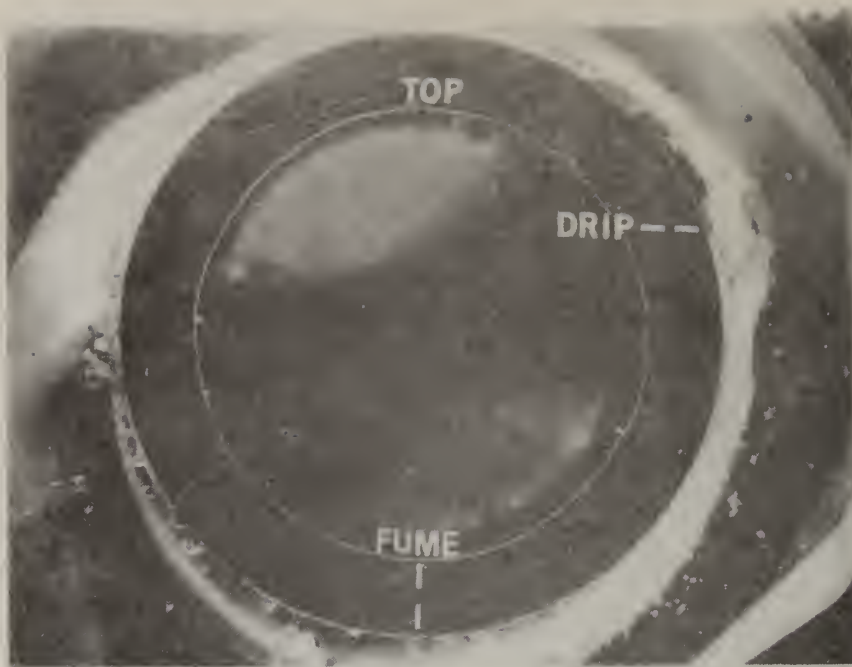


Fig. 23 Optical micrograph of a section of ASTM 213-22T steel tubing after exposure to a fuel rich hot gas stream seeded with  $K_2SO_4$ . Tube wall temperature  $400^\circ C$ .



Fig. 24 SEM photomicrograph 405x, of region, top, of optical micrograph, Fig. 18, showing reaction area at metal-salt interface. Lettered regions correspond to labeled EDX spectra Fig. 25-31.

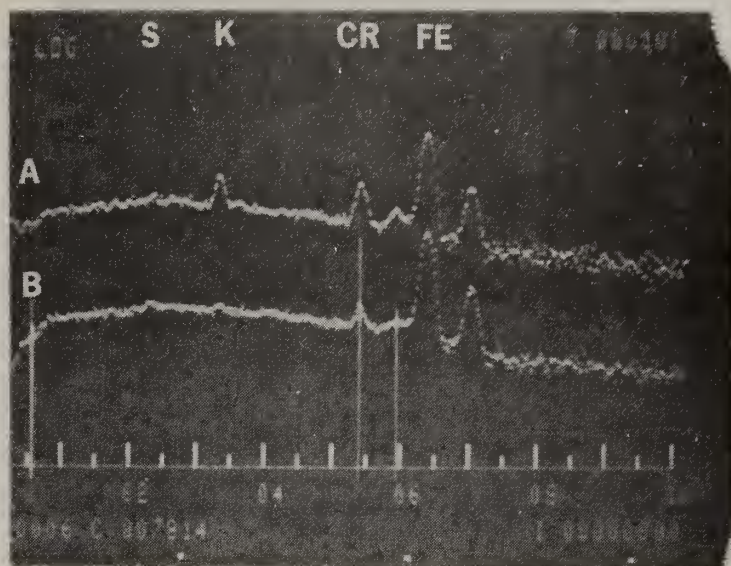


Fig. 25 EDX spectra of regions A and B of Fig. 24 showing high chromium concentration at bulk-reaction zone interface region. Specie positions and designations of all spectra in this section of the report are as indicated above.

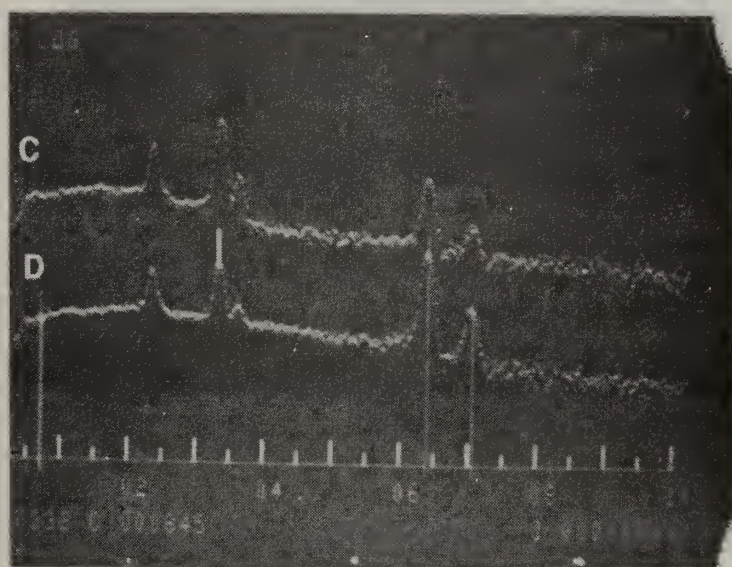


Fig. 26 EDX spectra of regions C and D of Fig. 24 showing depletion of chromium at salt-reaction zone interface region.

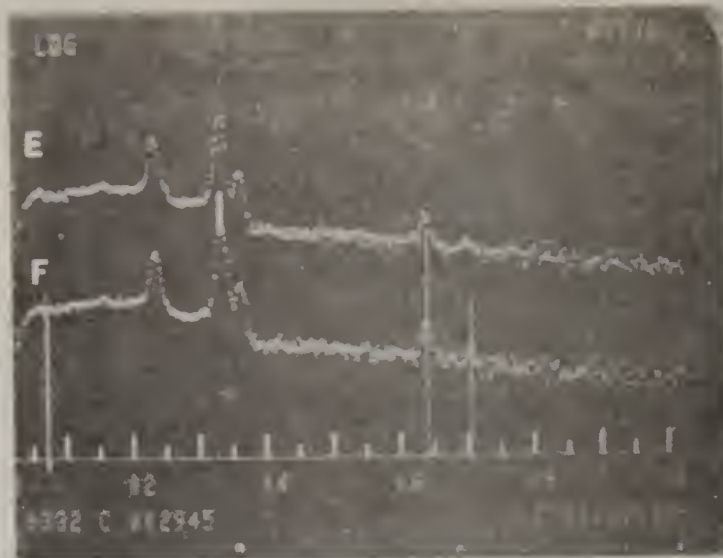


Fig. 27 EDX spectra of regions E and F of Fig. 24 showing penetration of iron into the salt coating.



Fig. 28 EDX spectra of regions G and H of Fig. 24 showing limit of iron penetration into the salt coating.

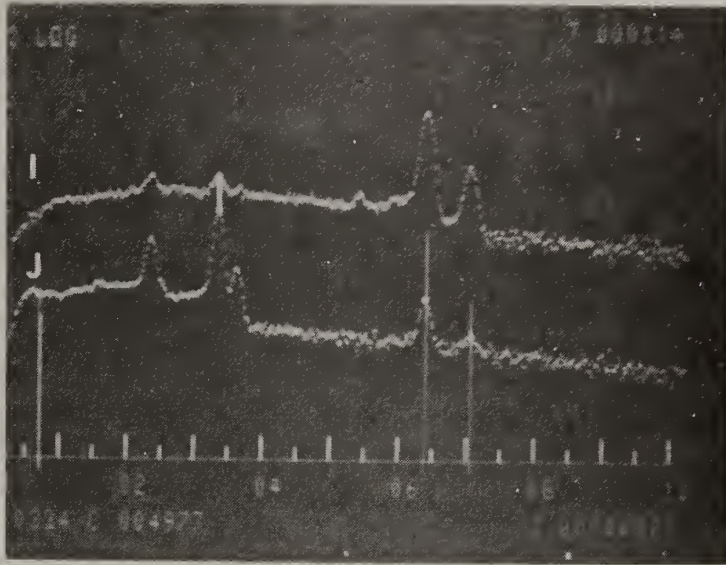


Fig. 29 EDX spectra of regions I and J of Fig. 24 showing depletion of chromium in the reaction zone--salt deposit interface region.

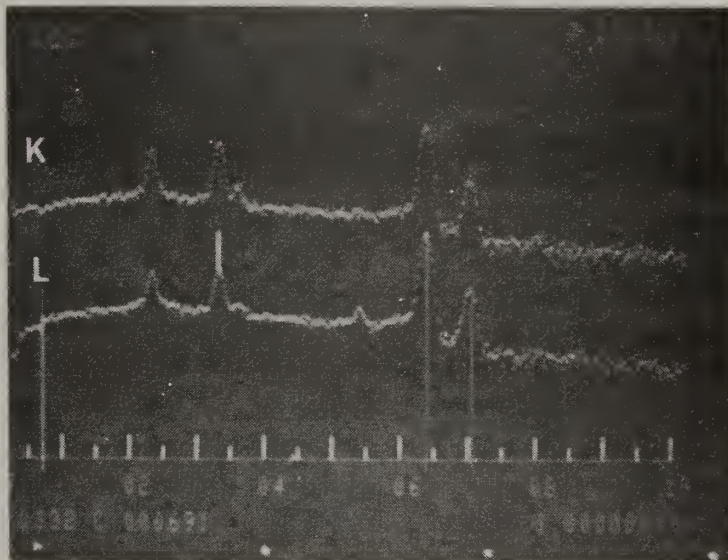


Fig. 30 EDX spectra of regions K and L of Fig. 24 showing depletion of chromium in the reaction zone--salt deposit interface region.

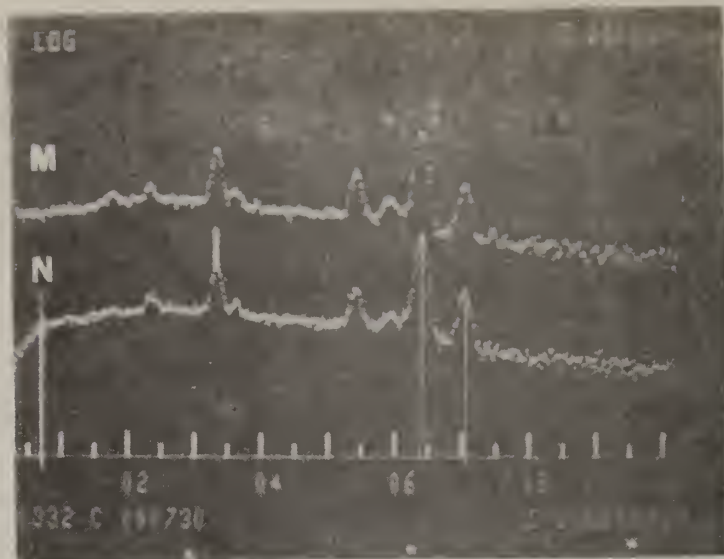
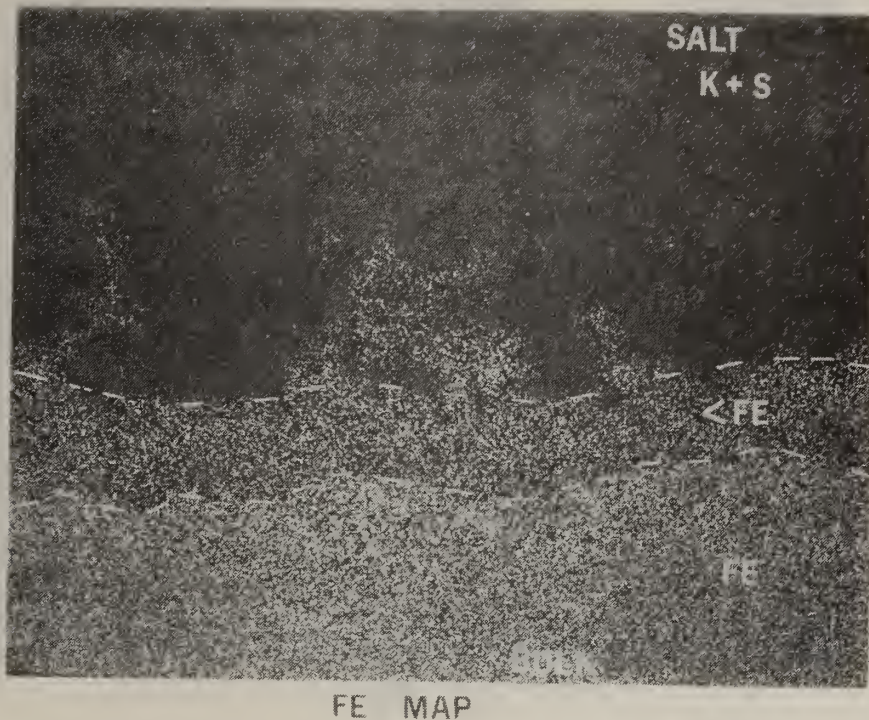


Fig. 31 EDX spectra of regions M and N of Fig. 24 showing potassium penetration into the bulk-reaction zone interface region.



Fig. 32 SEM photomicrograph 830x, of mid region of Fig. 24. Figs. 33-36 are specie maps of area of Fig. 32.



FE MAP

Fig. 33 EDX specie map of region shown in SEM photomicrograph Fig. 32, showing distribution of iron.



K MAP

Fig. 34 EDX specie map of region shown in SEM photomicrograph, Fig. 32, showing distribution of potassium.



Fig. 35 EDX specie map of region shown in SEM photomicrograph, Fig. 32, showing distribution of chromium.



Fig. 36 EDX specie map of region shown in SEM photomicrograph, Fig. 32, showing distribution of sulfur.

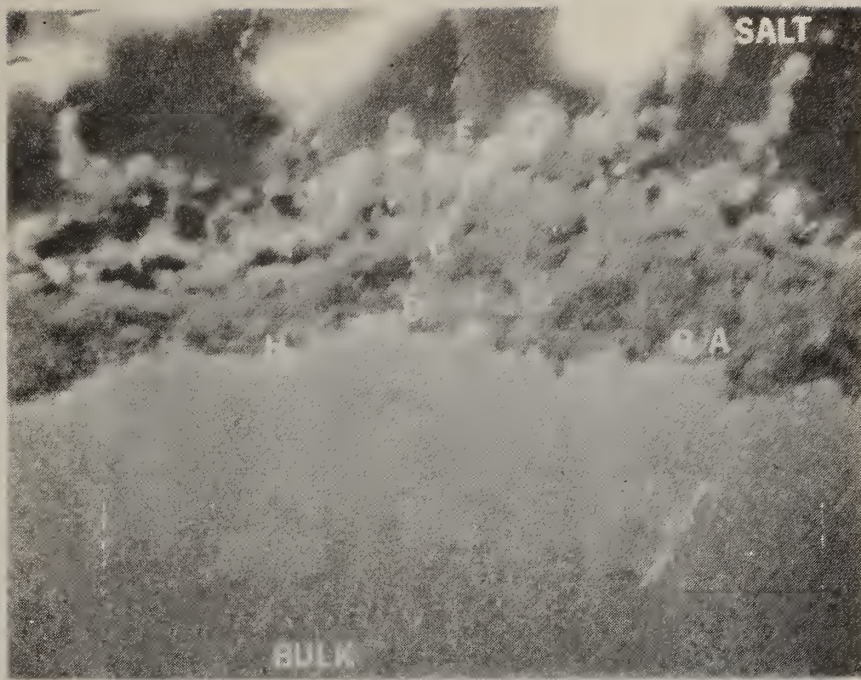


Fig. 37 SEM photomicrograph 1650x, of top region of Fig. 18 showing corrosion zone. Lettered region correspond to labeled EDX spectra Fig. 38-41.

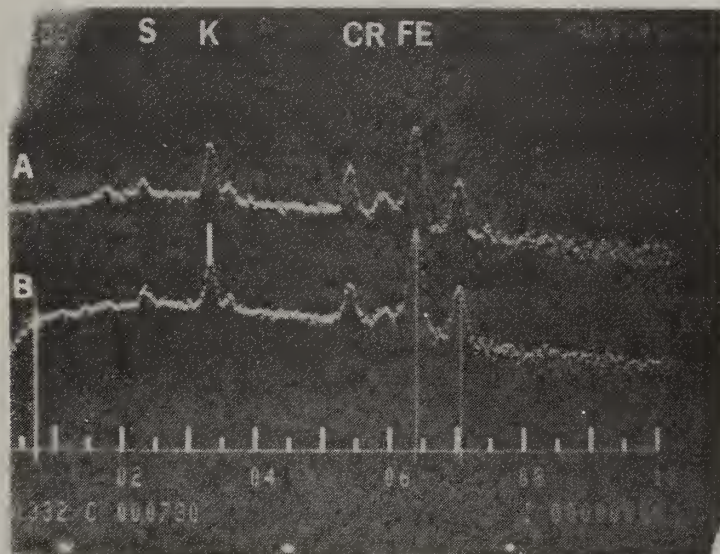


Fig. 38 EDX spectra of regions A and B of Fig. 37 showing high chromium peak at the bulk--corrosion zone interface.

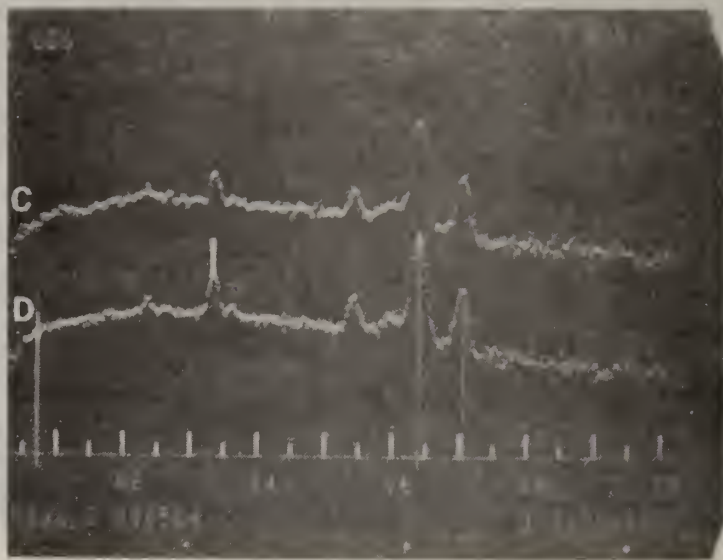


Fig. 39 EDX spectra of regions C and D of Fig. 37 showing potassium in the corrosion zone.

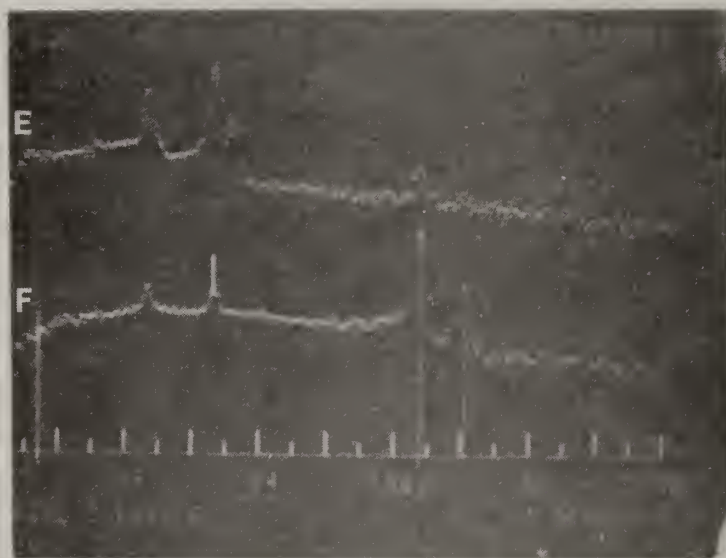


Fig. 40 EDX spectra of region E and F of Fig. 37 showing iron penetration into the salt coating.

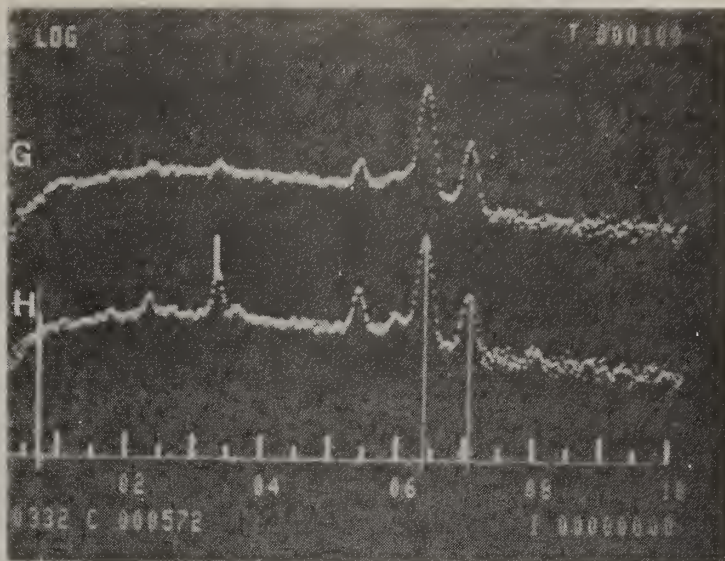


Fig. 41 EDX spectra of regions G and H of Fig. 37 showing high chromium peak at bulk-corrosion band interface.

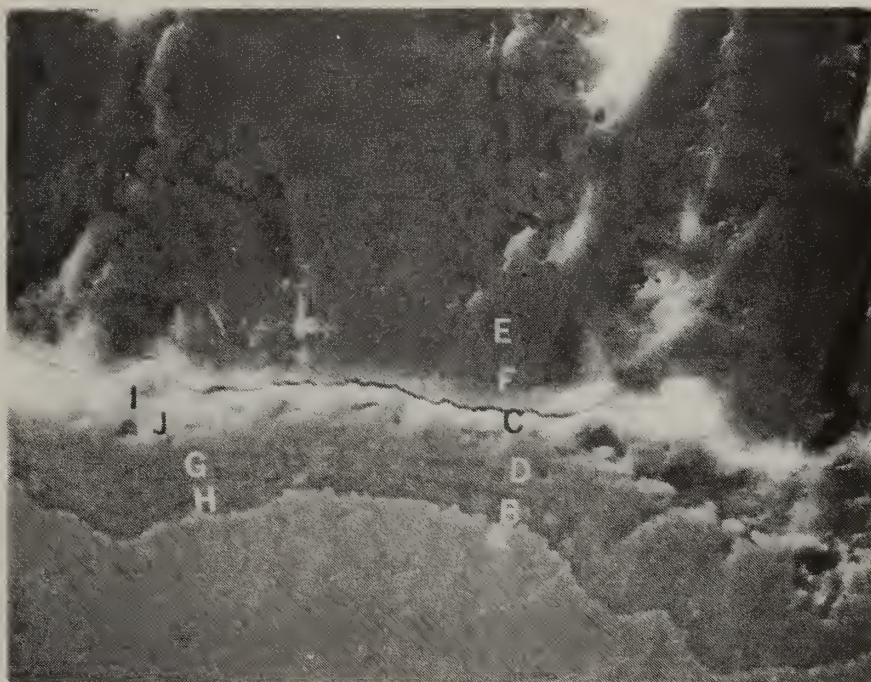


Fig. 42 SEM photomicrograph 840x, of drip zone region of Fig. 18 showing corrosion zone. Lettered regions correspond to labeled EDX spectra Figs. 43-47.



Fig. 43 EDX spectra of region A and B of Fig. 42 showing high chromium peak at bulk-corrosion zone interface.

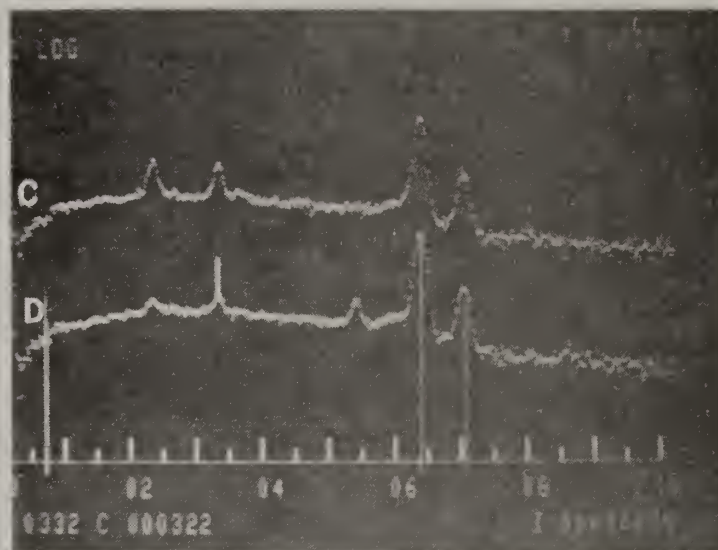


Fig. 44 EDX spectra of regions C and D of Fig. 42 showing chromium depletion at corrosion zone-salt deposit interface.

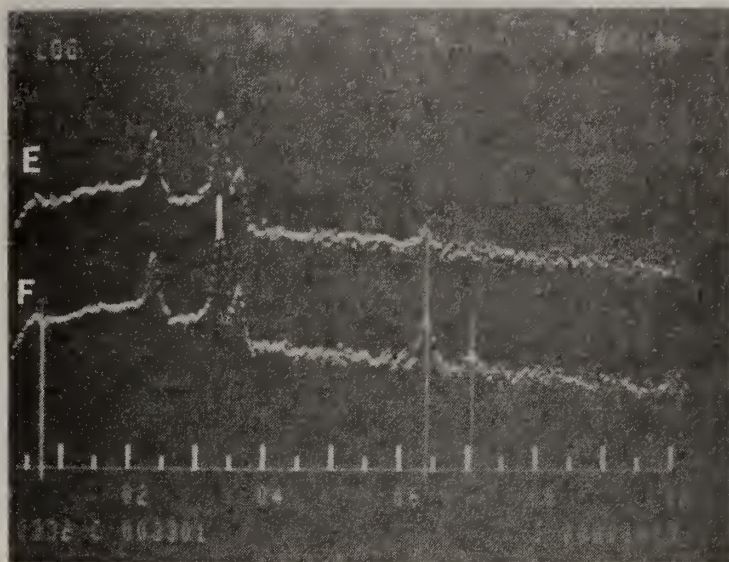


Fig. 45 EDX spectra of regions E and F of Fig. 42 showing iron penetration into the salt deposit.

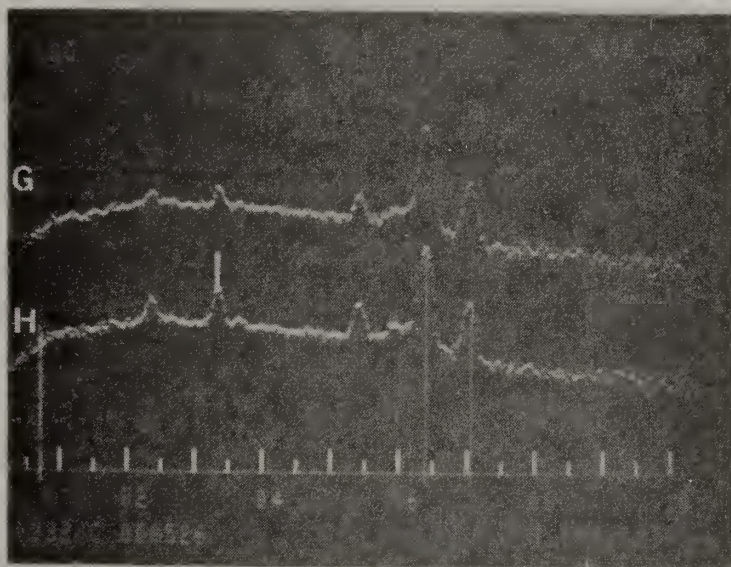


Fig. 46 EDX spectra of regions G and H of Fig. 42 showing potassium penetration into the corrosion zone.

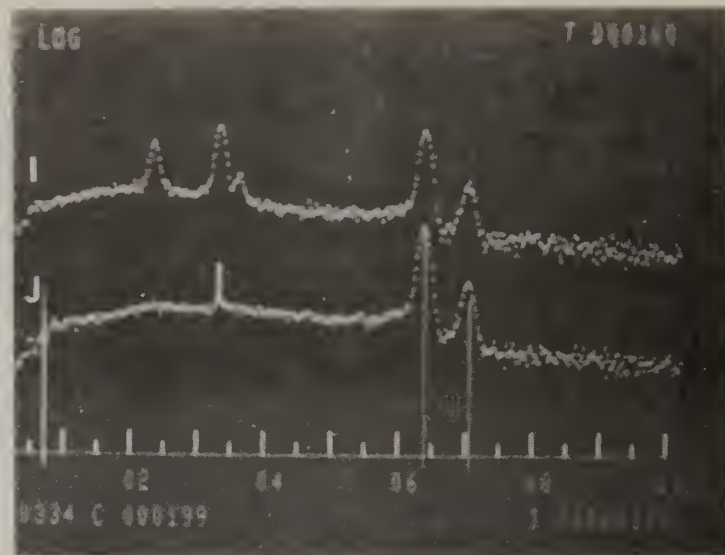


Fig. 47 EDX spectra of regions I and J of Fig. 42 showing iron penetration at the salt deposit-corrosion zone interface.



Fig. 48 SEM photomicrograph 435x, of fume deposit region of Fig. 18 showing corrosion zone. Figs. 49 and 50 are specie maps of the area of Fig. 48. Lettered regions correspond to labeled EDX spectra, Fig. 51 and 52.

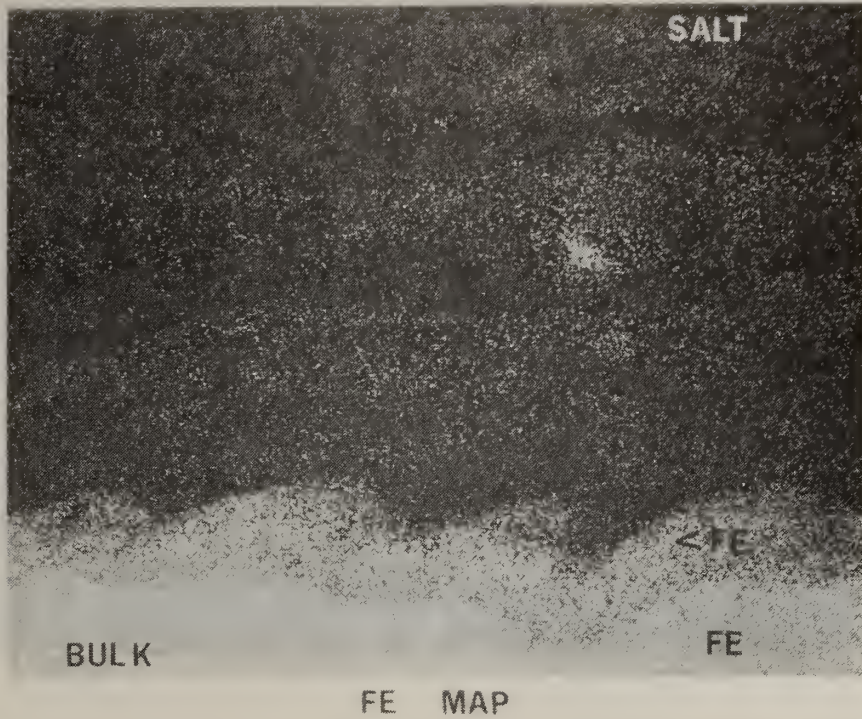


Fig. 49 EDX specie map of region shown in SEM micrograph Fig. 48 showing distribution of iron.

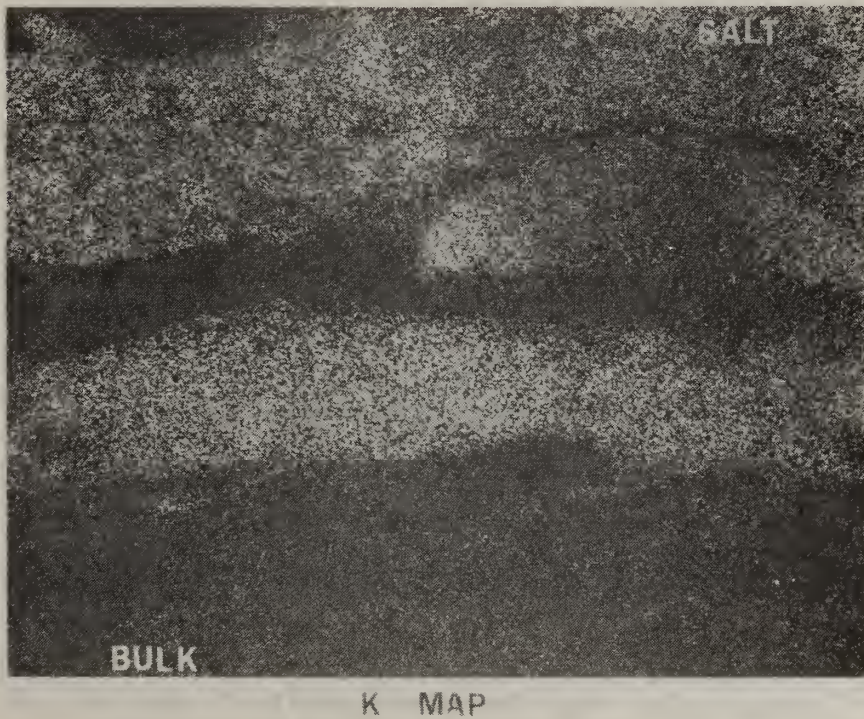


Fig. 50 EDX specie map of region shown in SEM micrograph Fig. 48 showing distribution of potassium.



Fig. 51 EDX spectra of regions A and B of Fig. 48 showing chromium depletion in the corrosion zone.

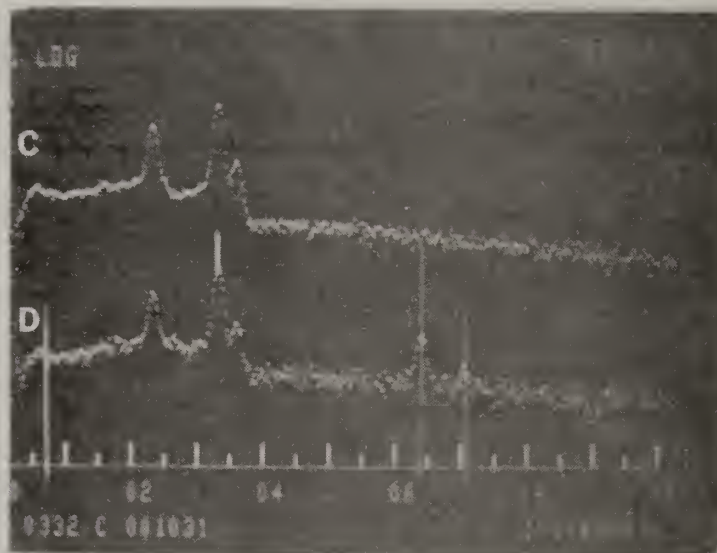


Fig. 52 EDX spectra of regions C and D of Fig. 48 showing iron penetration into the fume deposit.



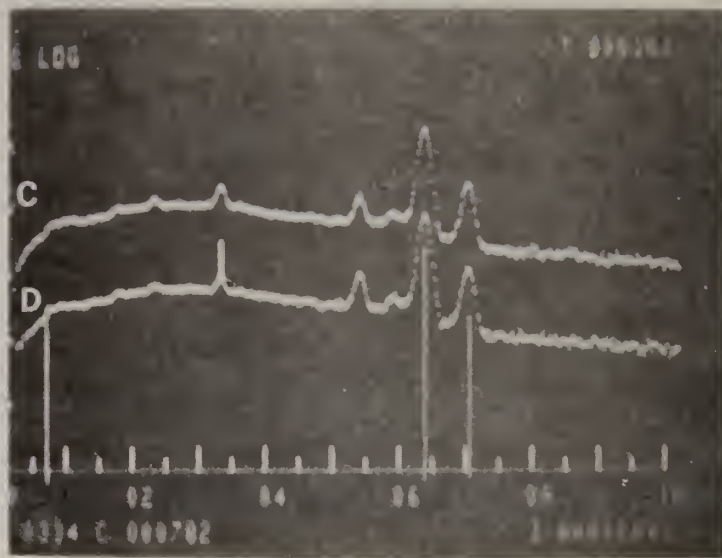


Fig. 55 EDX spectra of regions C and D of Fig. 53 showing potassium penetration in the corrosion zone.

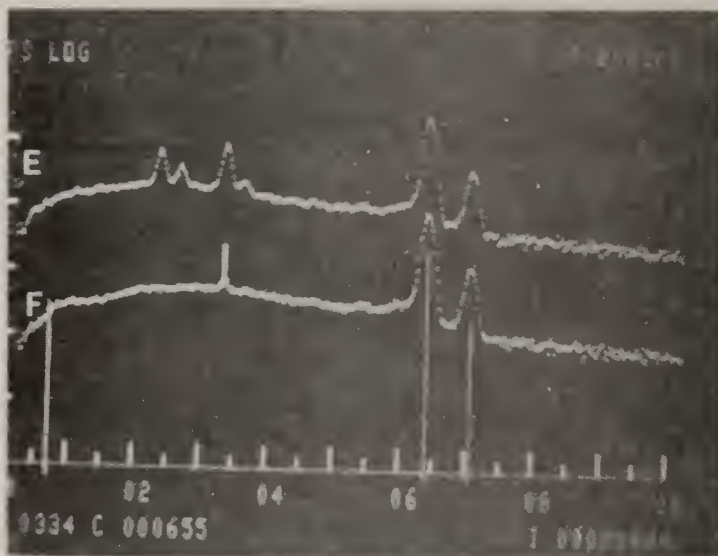


Fig. 56 EDX spectra of regions E and F of Fig. 53 showing chromium depletion at corrosion zone-salt deposit interface.

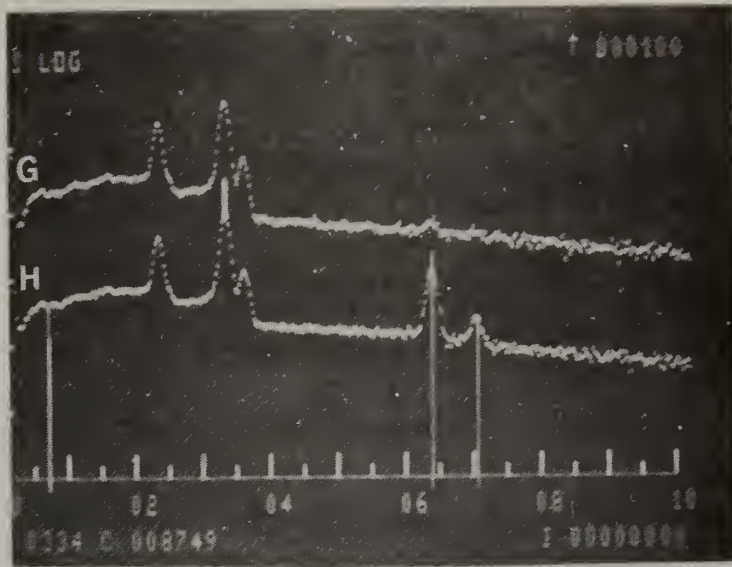


Fig. 57 EDX spectra of regions G and H of Fig. 53 showing iron penetration into the salt deposit.

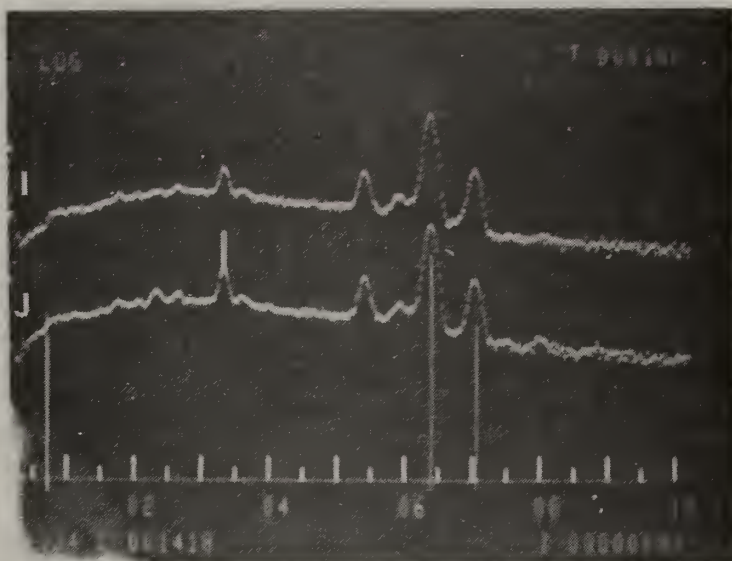


Fig. 58 EDX spectra of regions I and J of Fig. 53 showing potassium penetration into the corrosion zone.

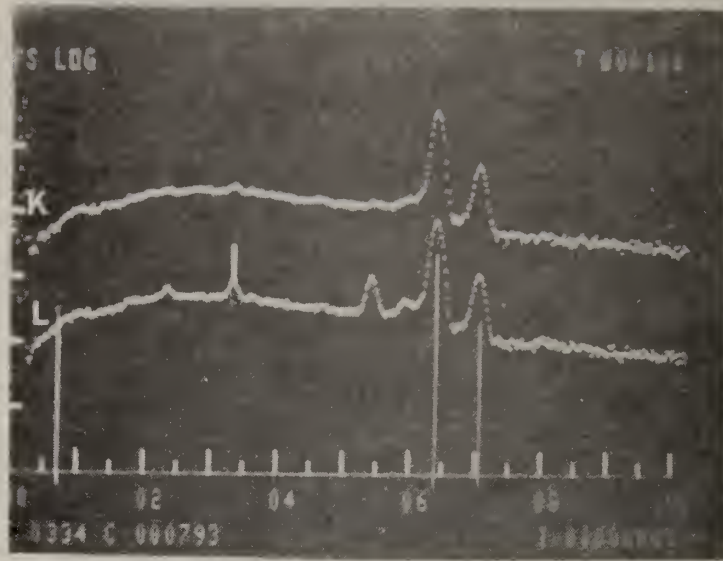


Fig. 59 EDX spectra of regions K and L of Fig. 53 showing chromium depletion in mid region of the corrosion zone.

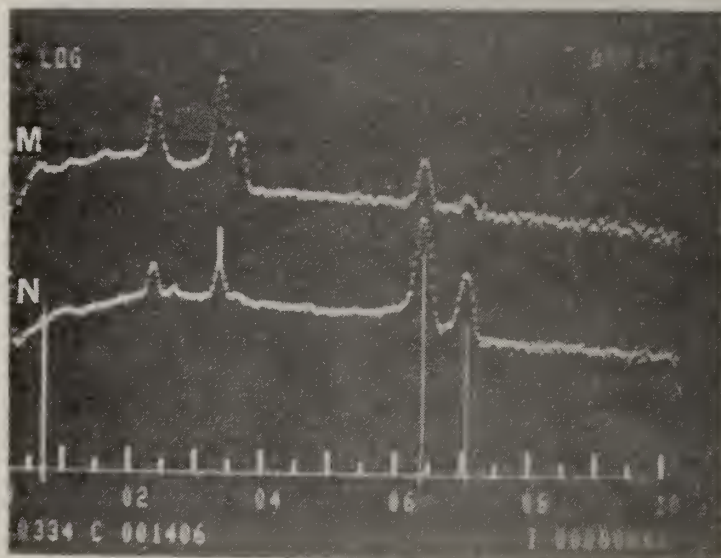


Fig. 60 EDX spectra of regions M and N of Fig. 53 showing iron penetration into the salt deposit.



Fig. 61 SEM photomicrograph 1070x, of drip zone region of Fig. 21 showing corrosion band.

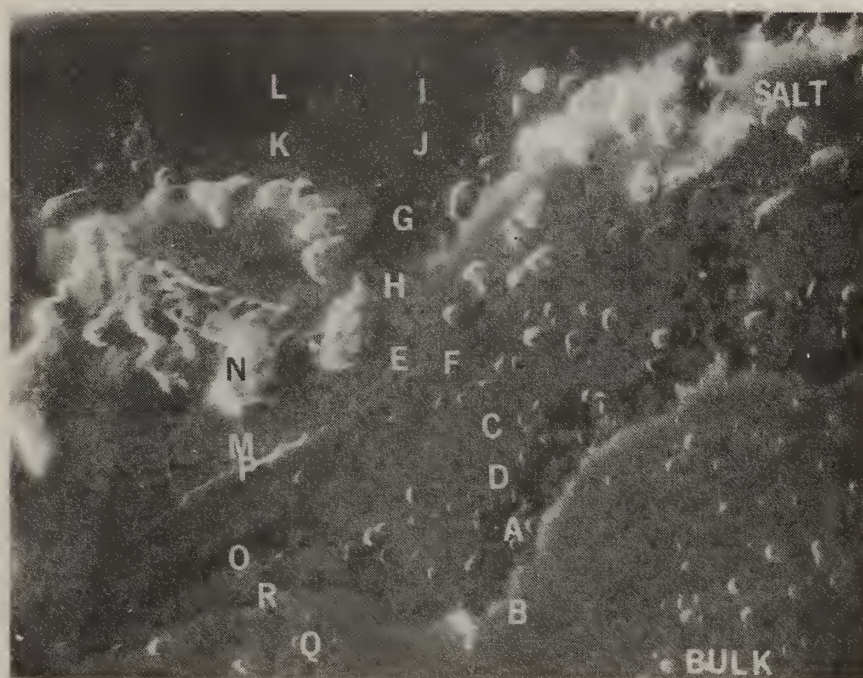


Fig. 62 SEM photomicrograph 2120x, of mid region of Fig. 61 showing corrosion band. Lettered regions correspond to labeled EDX 63-71.

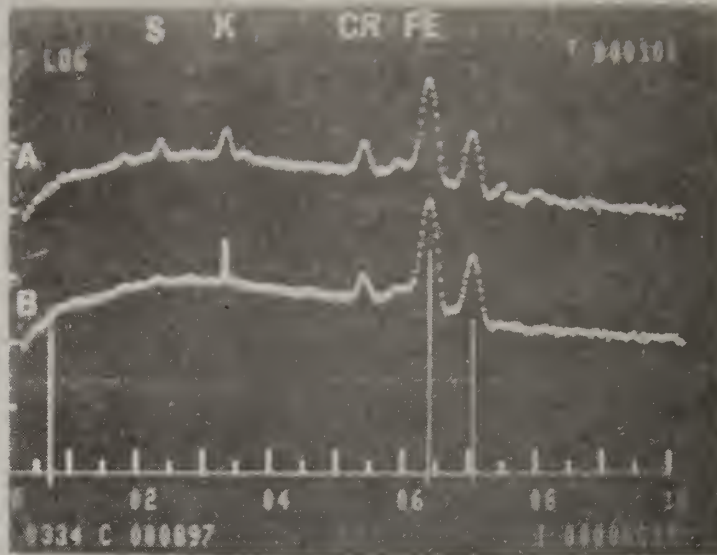


Fig. 63 EDX spectra of regions A and B of Fig. 62 showing high chromium peak at bulk-corrosion zone interface.

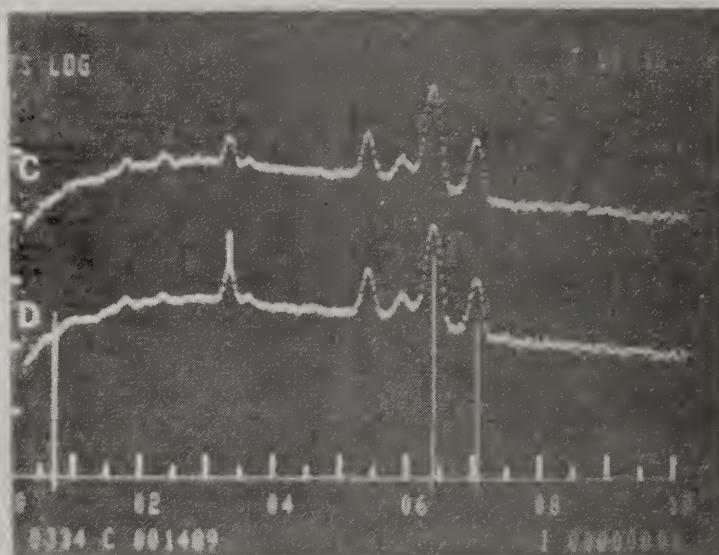


Fig. 64 EDX spectra of regions C and D of Fig. 62 showing potassium penetration into the corrosion zone.

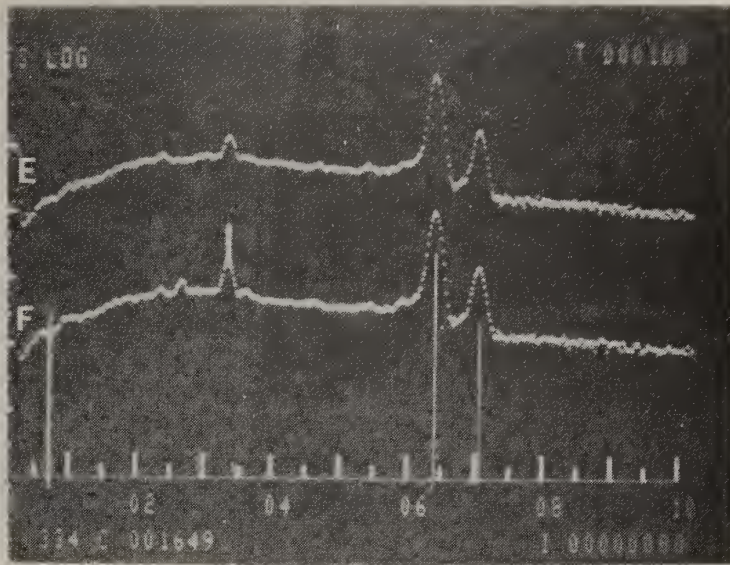


Fig. 65 EDX spectra of regions E and F of Fig. 62 showing chromium depletion at the corrosion zone-salt deposit interface,

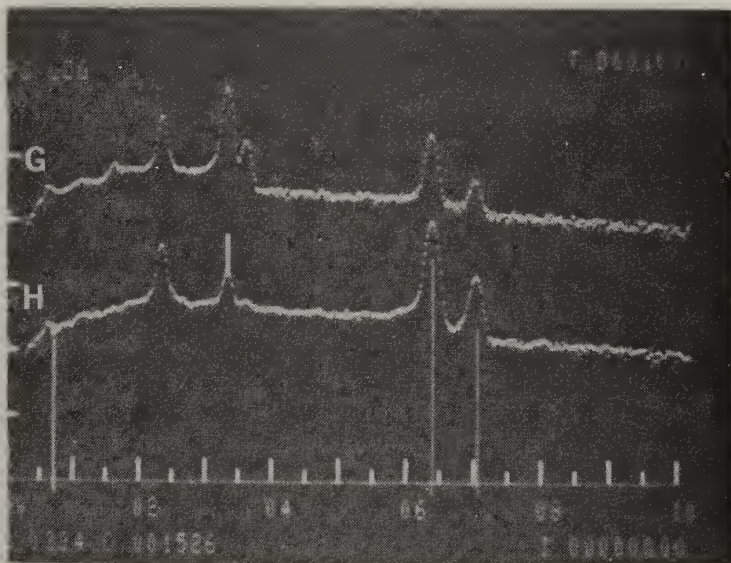


Fig. 66 EDX spectra of regions G and H of Fig. 62 showing iron penetration into the salt deposit.

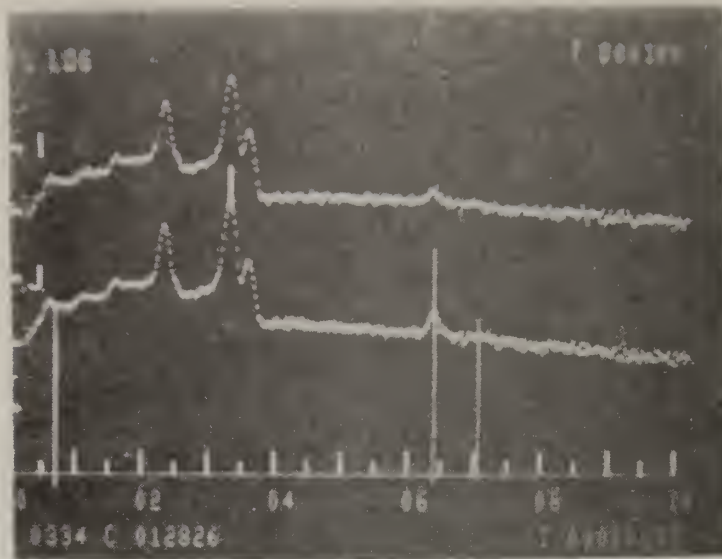


Fig. 67 EDX spectra of regions I and J of Fig. 62 showing iron penetration into the salt deposit.

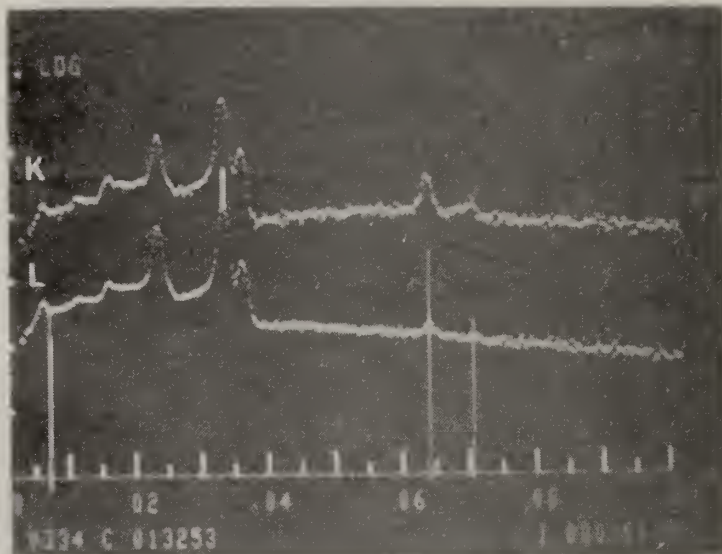


Fig. 68 EDX spectra of regions K and L of Fig. 62 showing iron penetration into the salt deposit.

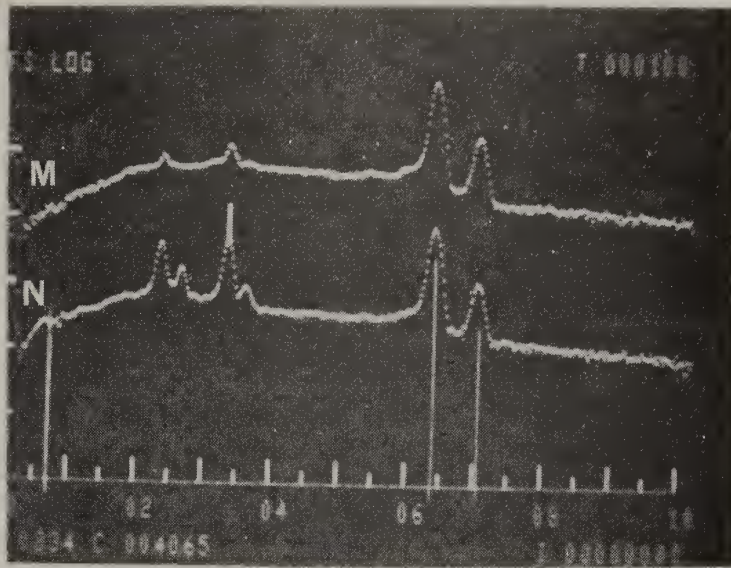


Fig. 69 EDX spectra of regions M and N of Fig. 62 showing iron penetration at the corrosion zone-salt deposit interface.

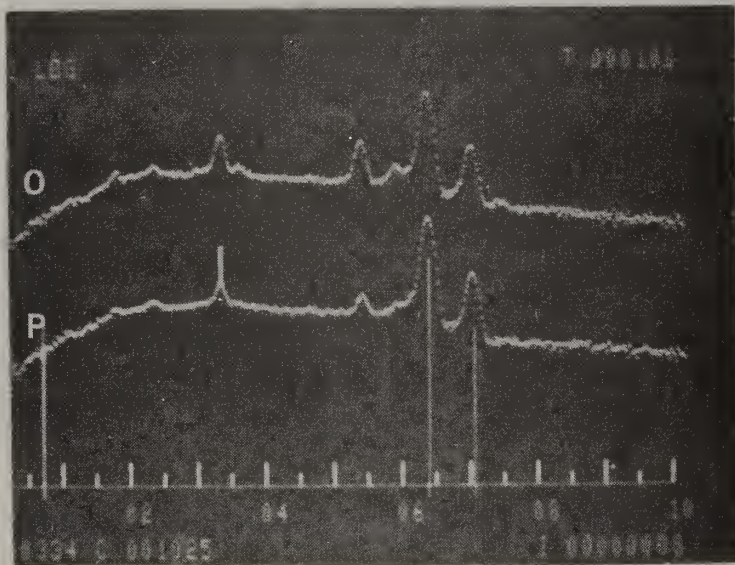


Fig. 70 EDX spectra of regions O and P of Fig. 62 showing chromium depletion in the corrosion zone.

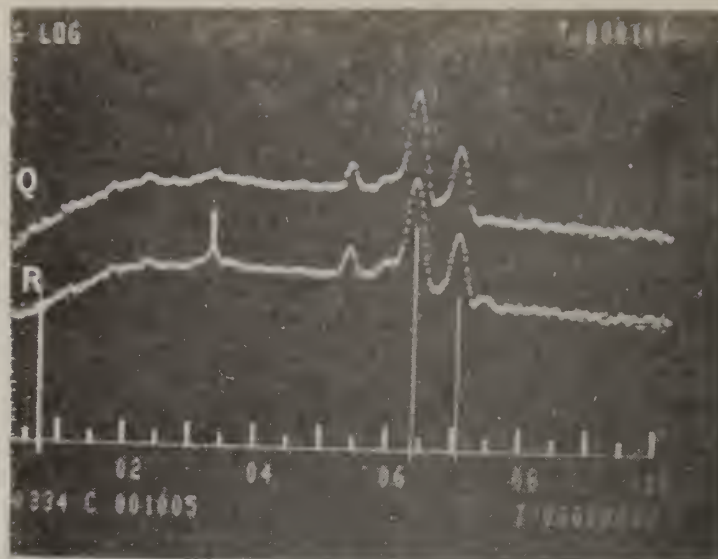


Fig. 71 EDX spectra of regions Q and R of Fig. 62 showing potassium at the bulk-corrosion zone interface.



Fig. 72 SEM photomicrograph 545x, of fume deposit region of Fig. 21 showing separation of corrosion band. Figs. 73-76 are specie maps of the area of Fig. 72.

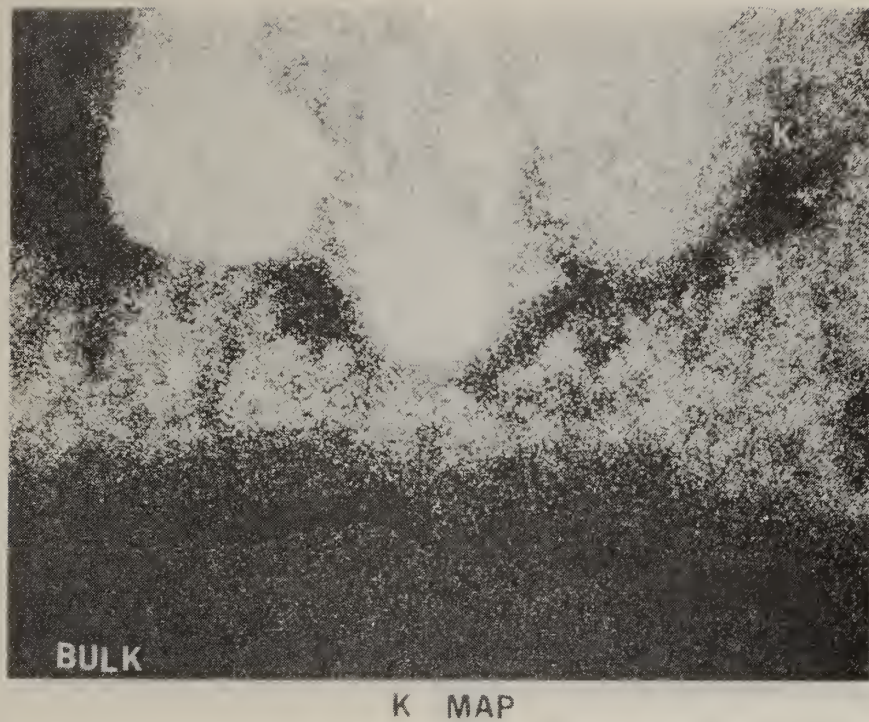


Fig. 73 EDX specie map of region shown in SEM photomicrograph Fig. 72 showing distribution of potassium.

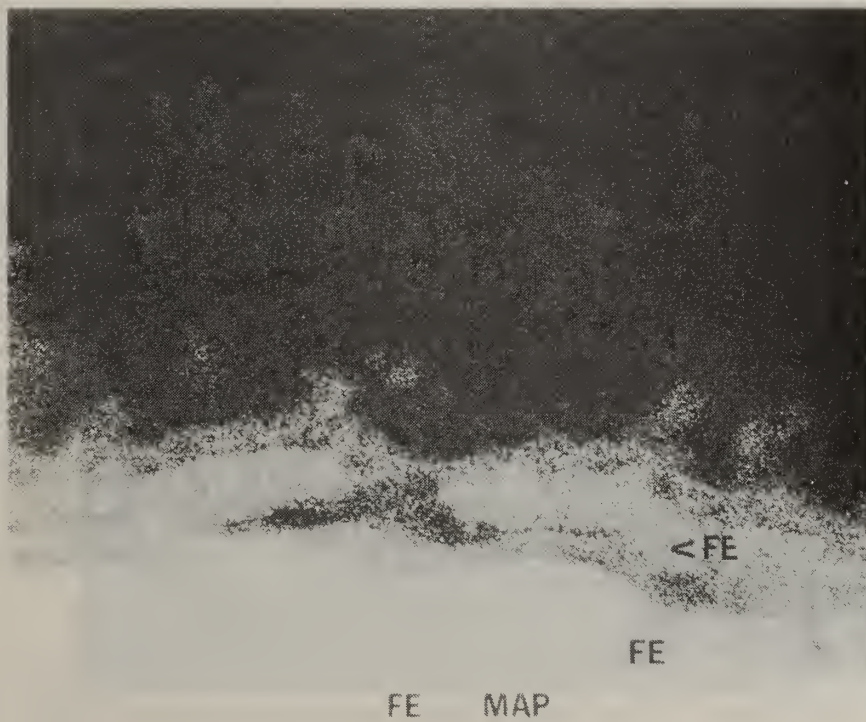


Fig. 74 EDX specie map of region shown in SEM photomicrograph Fig. 72 showing distribution of iron.



Fig. 75 EDX specie map of region shown in SEM photomicrograph Fig. 72 showing distribution of sulfur.



Fig. 76 EDX specie map of region shown in SEM photomicrograph Fig. 72 showing distribution of chromium.



Fig. 77 SEM photomicrograph of 1050x, of mid region of Fig. 72. Lettered regions correspond to labeled EDX spectra Figs. 78-86.

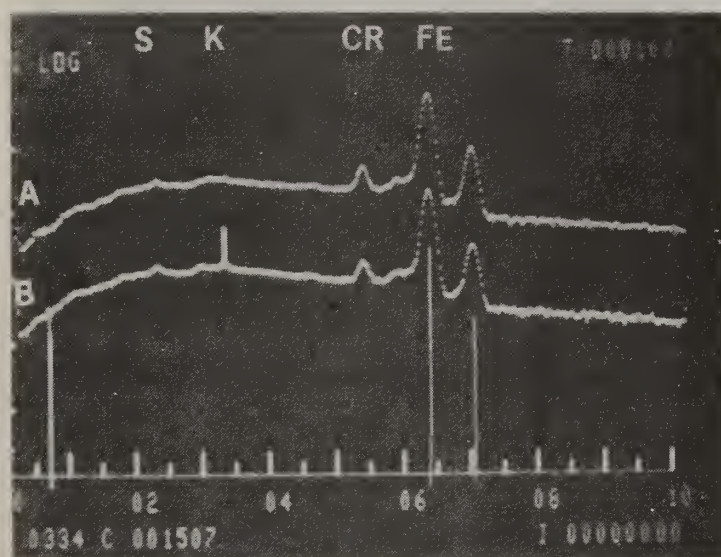


Fig. 78 EDX spectra of regions A and B of Fig. 77 showing chromium peak in the bulk.

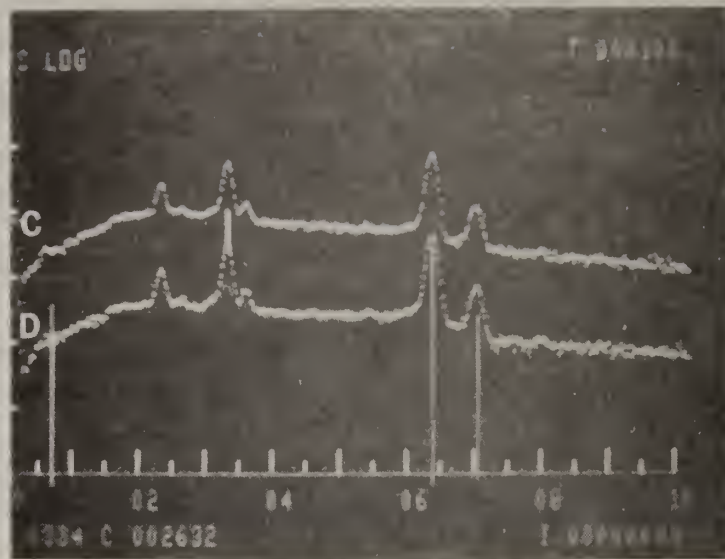


Fig. 79 EDX spectra of regions C and D of Fig. 77 showing chromium depletion in the corrosion zone.

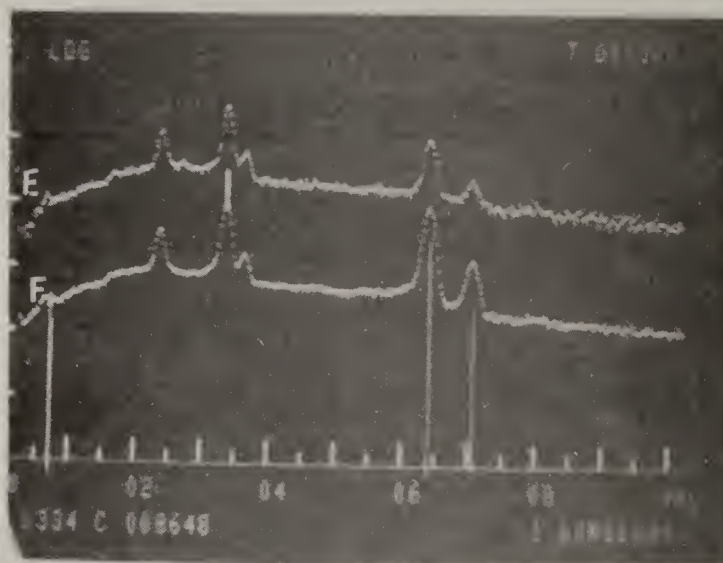


Fig. 80 EDX spectra of region E and F of Fig. 77 showing iron penetration into the fume deposit.

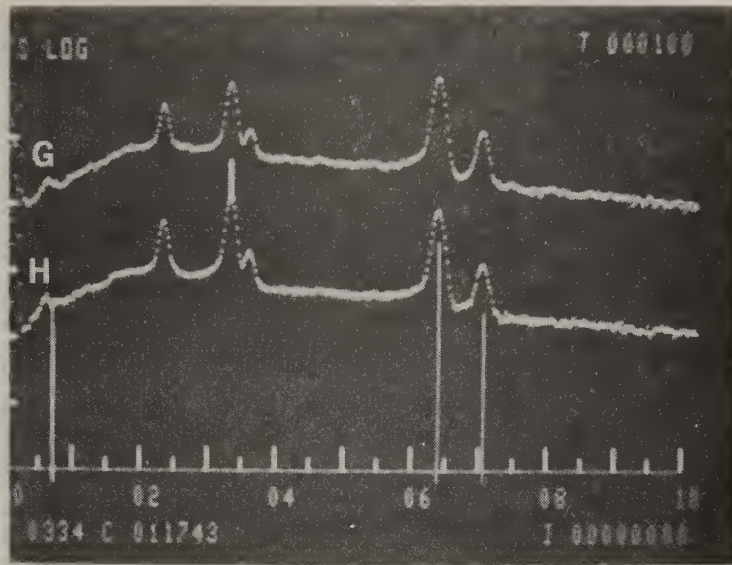


Fig. 81 EDX spectra of regions G and H of Fig. 77 showing iron penetration into the fume deposit.

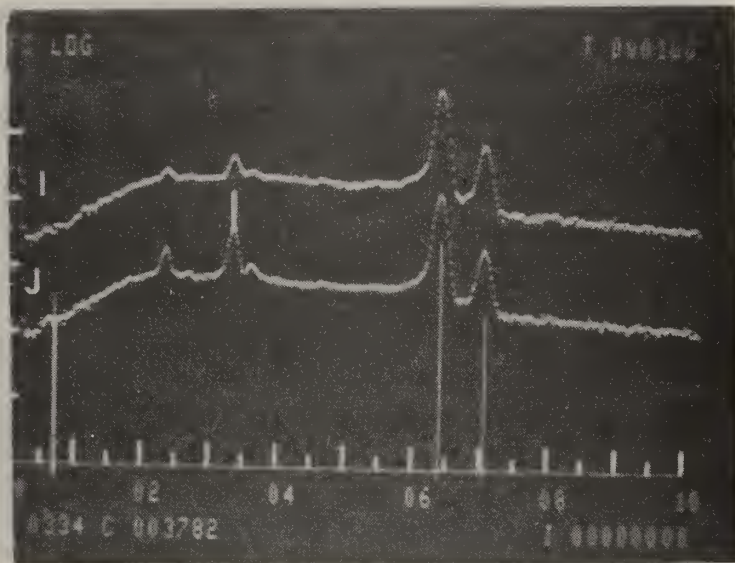


Fig. 82 EDX spectra of regions I and J of Fig. 77 showing chromium depletion at corrosion zone-fume deposit interface.

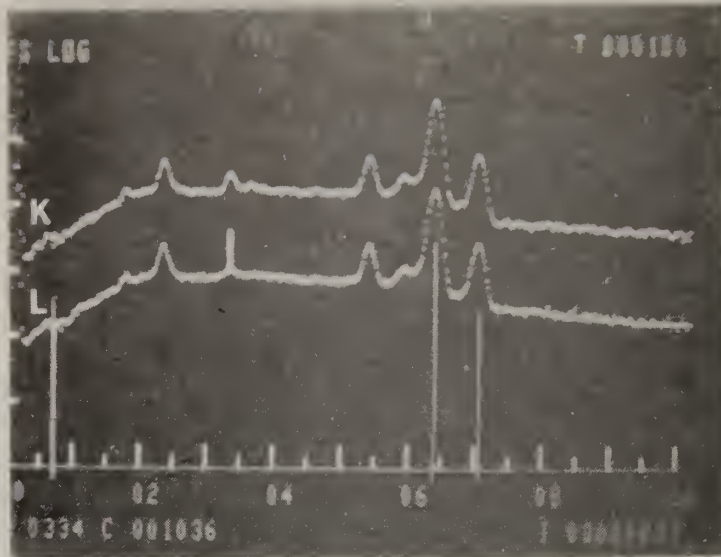


Fig. 83 EDX spectra of regions K and L of Fig. 77 showing high chromium peaks at the corrosion zone-fume deposit interface.

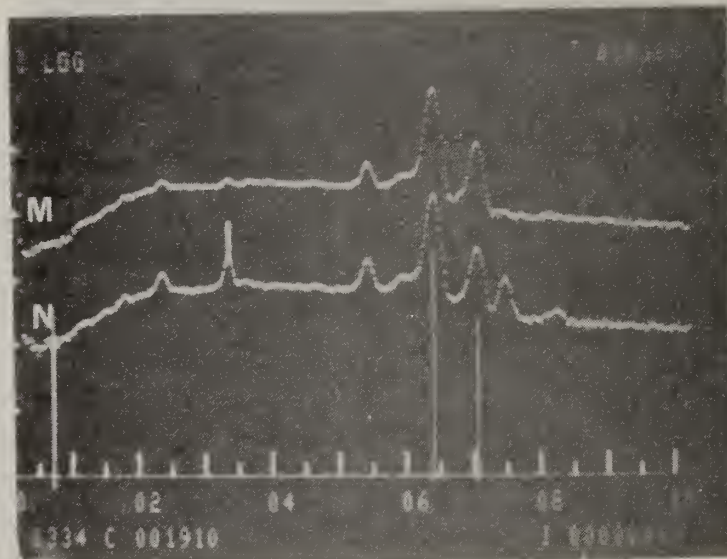


Fig. 84 EDX spectra of regions M and N of Fig. 77 showing potassium penetration at the bulk-corrosion zone interface.

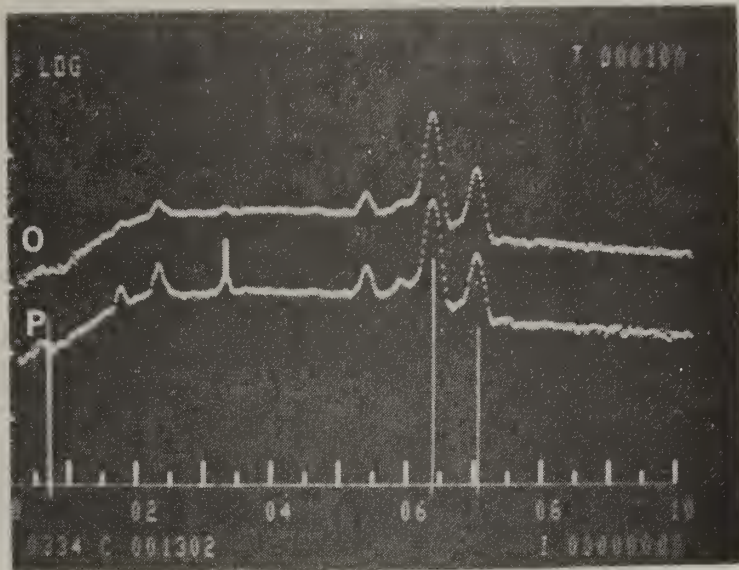


Fig. 85 EDX spectra of regions O and P of Fig. 77 showing potassium penetration at the bulk-corrosion zone interface.

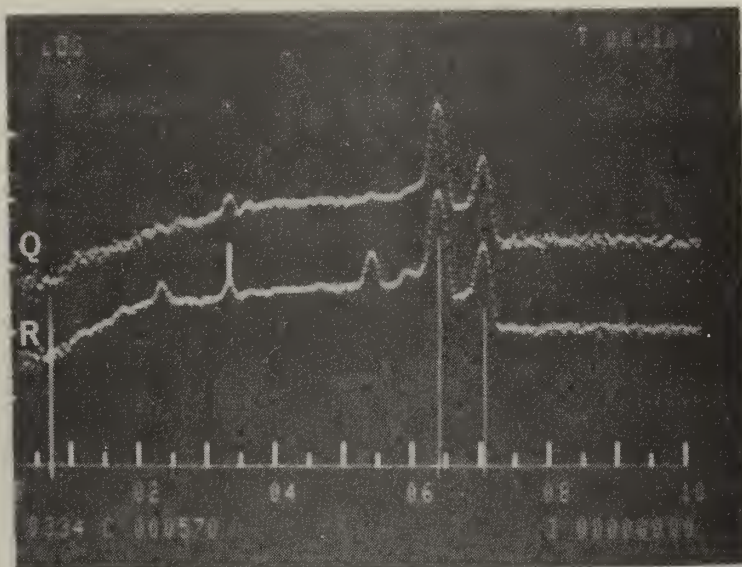


Fig. 86 EDX spectra of regions Q and R of Fig. 77 showing potassium and sulfur in the bulk-corrosion band break.

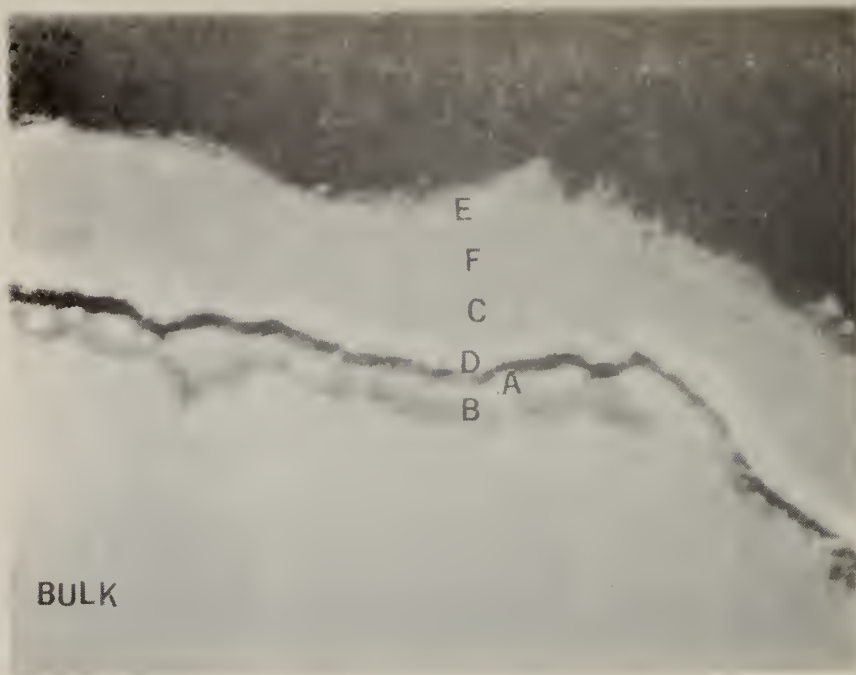


Fig. 87 SEM photomicrograph 1760x, of the top region of Fig. 19 showing separation in the corrosion band. Lettered regions correspond to labeled EDX spectra Figs. 80-90.

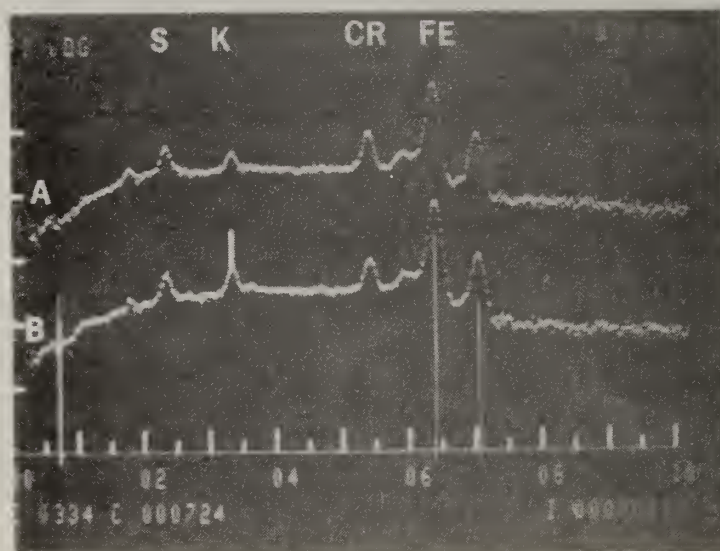


Fig. 88 EDX spectra of regions A and B of Fig. 87 showing high chromium peak and penetration of potassium and sulfur at the corrosion zone-bulk interface.

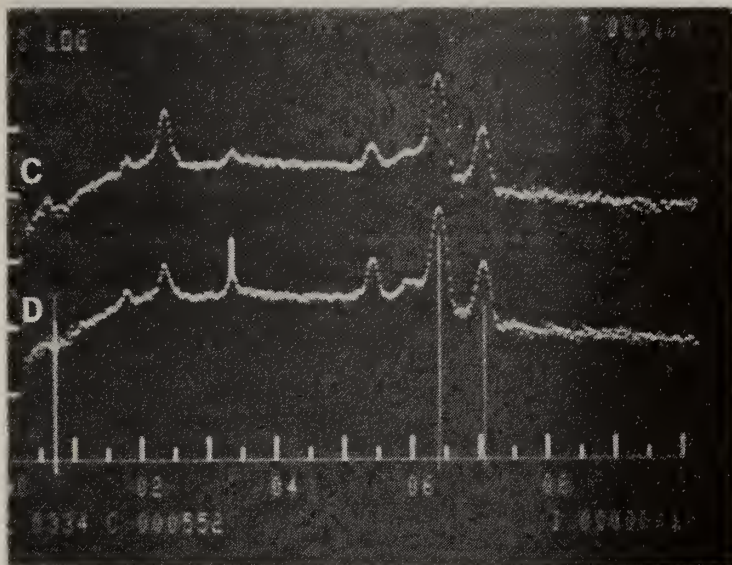


Fig. 89 EDX spectra of regions C and D of Fig. 88 showing high sulfur peaks in the mid corrosion band region.

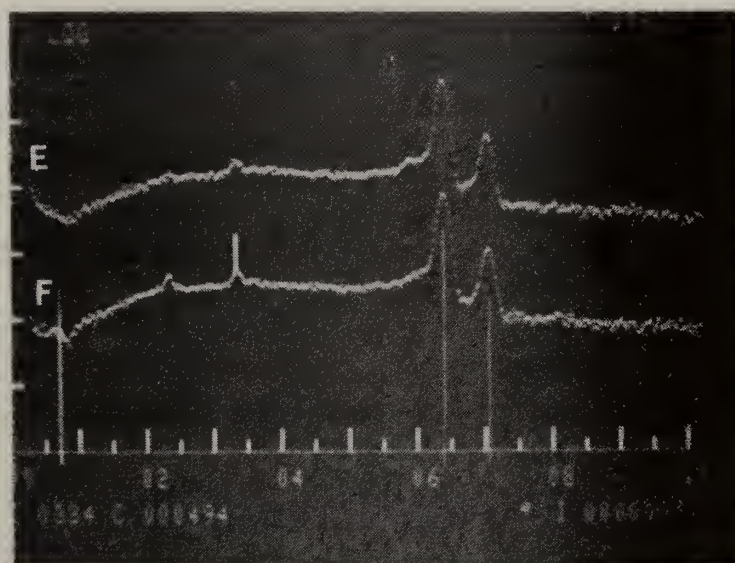


Fig. 90 EDX spectra of regions E and F of Fig. 88 showing chromium depletion in the upper portion of the corrosion zone.



Fig. 91 SEM photomicrograph 1000x, of drip zone region of Fig. 22 showing corrosion zone. Lettered regions correspond to labeled EDX spectra Figs. 92-97.

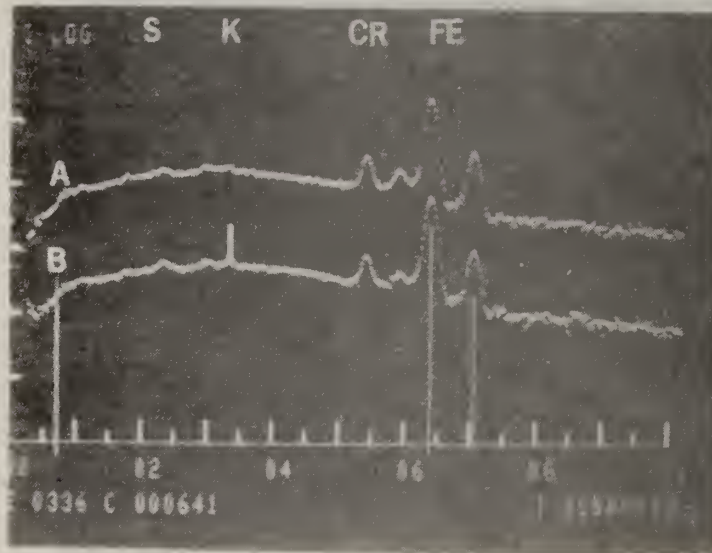


Fig. 92 EDX spectra of regions A and B of Fig. 91 showing iron and chromium peaks at the bulk-corrosion zone interface.

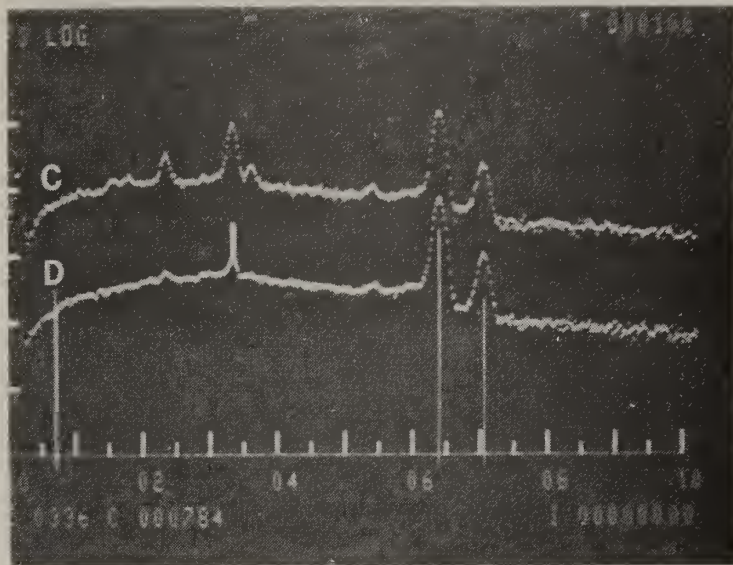


Fig. 93 EDX spectra of regions C and D of Fig. 91 showing depletion of chromium above bulk-corrosion zone interface.

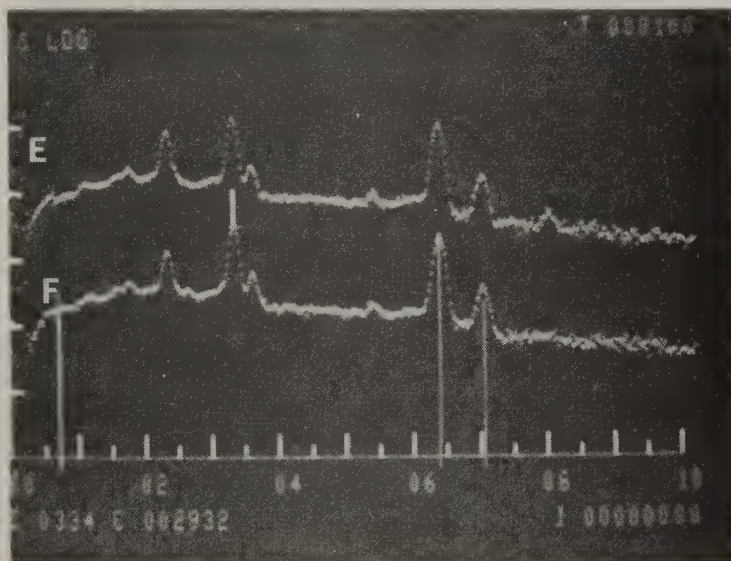
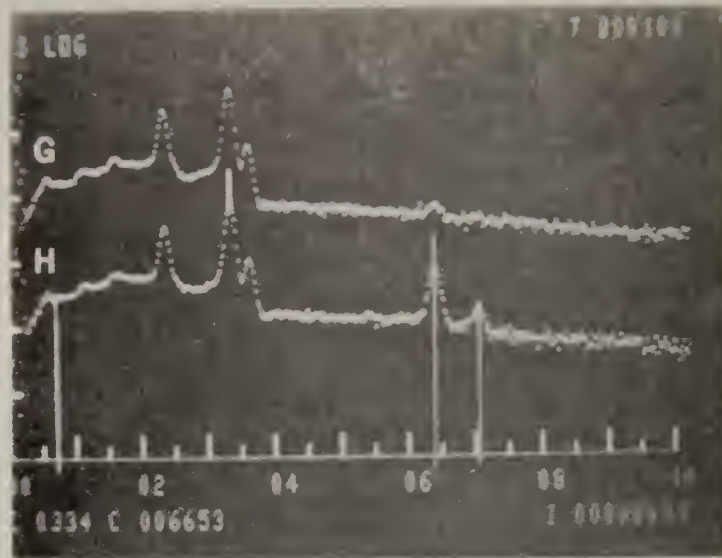
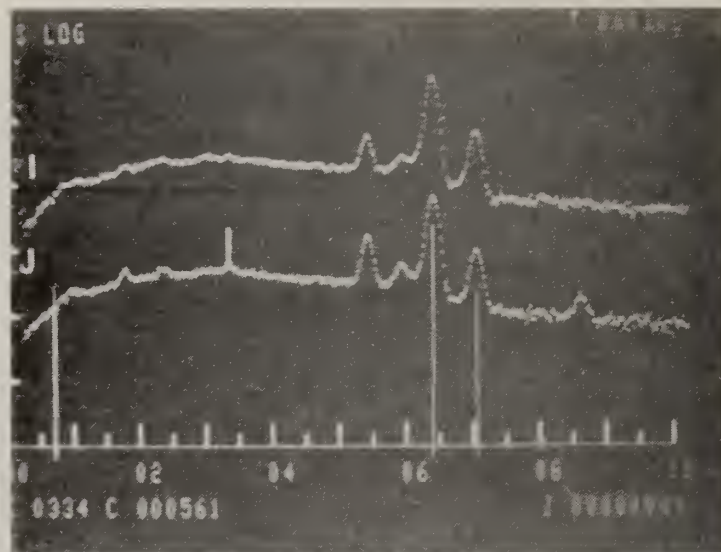


Fig. 94 EDX spectra of regions E and F of Fig. 91 showing sulfur and potassium penetration in the mid region of the corrosion band.



**Fig. 95** EDX spectra of regions G and H of Fig. 91 showing iron penetration in to the salt deposit.



**Fig. 96** EDX spectra of regions I and J of Fig. 91 showing high chromium peak at the bulk-corrosion zone interface.

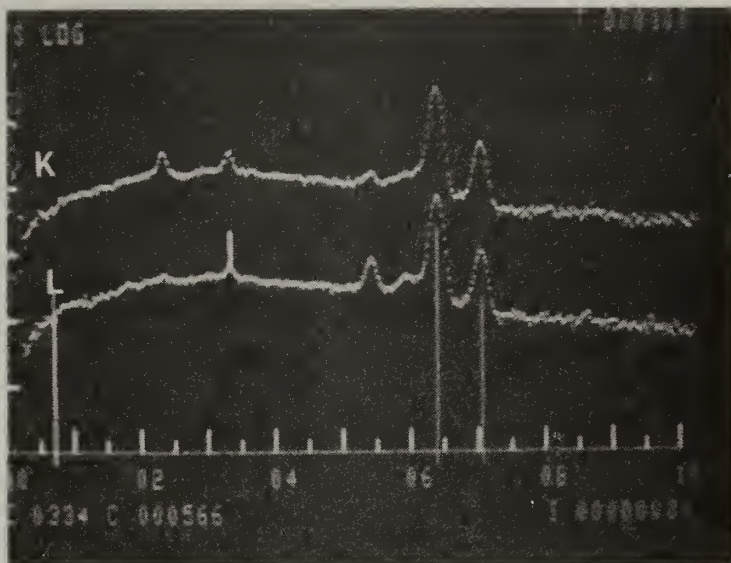


Fig. 97 EDX spectra of region K and L of Fig. 91 showing chromium depletion above region I and J.

